USGS
science for a changing world

System Characterization Report on Tanager

Chapter W of
System Characterization of Earth Observation Sensors

Open-File Report 2021–1030–W

U.S. Department of the Interior
U.S. Geological Survey

System Characterization Report on Tanager

By Minsu Kim,[1] Seonkyung Park,[2] Cody Anderson,[3] Jeff Clauson,[3] Jim Vrabel,[1] and Ajit Sampath[1]

Chapter W of
System Characterization of Earth Observation Sensors

Compiled by Shankar N. Ramaseri Chandra[1]

[1]KBR, Inc., under contract to the U.S. Geological Survey.

[2]USS, Inc., under contract to the U.S. Geological Survey.

[3]U.S. Geological Survey.

Open-File Report 2021–1030–W

U.S. Department of the Interior
U.S. Geological Survey

U.S. Geological Survey, Reston, Virginia: 2026

For more information on the USGS—the Federal source for science about the Earth, its natural and living resources, natural hazards, and the environment—visit https://www.usgs.gov.

For an overview of USGS information products, including maps, imagery, and publications, visit https://store.usgs.gov/.

Any use of trade, firm, or product names is for descriptive purposes only and does not imply endorsement by the U.S. Government.

Although this information product, for the most part, is in the public domain, it also may contain copyrighted materials as noted in the text. Permission to reproduce copyrighted items must be secured from the copyright owner.

Suggested citation:
Kim, M., Park, S., Anderson, C., Clauson, J., Vrabel, J., and Sampath, A., 2026, System characterization report on Tanager, chap. W *of* Ramaseri Chandra, S.N., ed., System characterization of Earth observation sensors: U.S. Geological Survey Open-File Report 2021–1030, 45 p., https://doi.org/10.3133/ofr20211030W.

Associated data for this publication:
Planet Labs PBC, 2026, Tanager—Cutting-edge hyperspectral from orbit: Planet Labs PBC website, accessed March 5, 2026, at https://www.planet.com/constellations/tanager/.

ISSN 2331-1258 (online)

Contents

Executive Summary....1
Introduction....1
System Description....2
    Satellite and Operational Details....2
    Sensor Information....2
Procedures....2
Measurements....3
Analysis....3
    Geometric Performance....3
        Band to Band....3
        Image to Image....10
    Radiometric Performance....10
    Comparison to Radiometric Calibration Network....36
    Spectral Shift....36
    Spatial Performance....36
Summary and Conclusions....45
Selected References....45

Figures

1. The Mojave Desert, Arizona, Planet Labs PBC Tanager scene used to compute band-to-band error....4
2. Graph showing relative band-to-band easting geometric error derived from the Mojave Desert, Arizona, Planet Labs PBC Tanager scene using band 38 as a reference....5
3. Graph showing relative band-to-band northing geometric error derived from the Mojave Desert, Arizona, Planet Labs PBC Tanager scene using band 38 as a reference....5
4. Graph showing relative band-to-band easting geometric error derived from the Indian Planet Labs PBC Tanager scene using band 38 as a reference....6
5. Graph showing relative band-to-band northing geometric error derived from the Indian Planet Labs PBC Tanager scene using band 38 as a reference....6
6. Graph showing relative band-to-band easting geometric error derived from the Sudanese Planet Labs PBC Tanager scene using band 38 as a reference....7
7. Graph showing relative band-to-band northing geometric error derived from the Sudanese Planet Labs PBC Tanager scene using band 38 as a reference....7
8. Graph showing relative band-to-band easting geometric error derived from the Australian Planet Labs PBC Tanager scene using band 38 as a reference....8
9. Graph showing relative band-to-band northing geometric error derived from the Australian Planet Labs PBC Tanager scene using band 38 as a reference....8
10. Graph showing relative band-to-band easting geometric error derived from the Chinese Planet Labs PBC Tanager scene using band 38 as a reference....9
11. Graph showing relative band-to-band northing geometric error derived from the Chinese Planet Labs PBC Tanager scene using band 38 as a reference....9

12. Image-to-image geometric error map with error vector for each grid using the Mojave Desert, Arizona, scene pair comprising a Planet Labs PBC Tanager scene and a Landsat Operational Land Imager scene....11
13. Histogram of image-to-image geometric error derived from the Mojave Desert, Arizona, scene pair comprising a Planet Labs PBC Tanager scene and a Landsat Operational Land Imager scene....12
14. Error scatterplot of image-to-image geometric error derived from the Mojave Desert, Arizona, scene pair comprising a Planet Labs PBC Tanager scene and a Landsat Operational Land Imager scene....12
15. Image-to-image geometric error map with error vector for each grid derived from the Indian scene pair comprising a Planet Labs PBC Tanager scene and a Landsat Operational Land Imager scene....13
16. Histogram of image-to-image geometric derived from the Indian scene pair comprising a Planet Labs PBC Tanager scene and a Landsat Operational Land Imager scene....14
17. Error scatterplot of image-to-image geometric error derived from the Indian scene pair comprising a Planet Labs PBC Tanager scene and a Landsat Operational Land Imager scene....14
18. Image-to-image geometric error map with error vector for each grid derived from the Sudanese scene pair comprising a Planet Labs PBC Tanager scene and a Landsat Operational Land Imager scene....15
19. Histogram of image-to-image geometric error derived from the Sudanese scene pair comprising a Planet Labs PBC Tanager scene and a Landsat Operational Land Imager scene....16
20. Error scatterplot of image-to-image geometric error derived from the Sudanese scene pair comprising a Planet Labs PBC Tanager scene and a Landsat Operational Land Imager scene....16
21. Image-to-image geometric error map with error vector for each grid derived from the Australian scene pair comprising a Planet Labs PBC Tanager scene and a Landsat Operational Land Imager scene....17
22. Histogram of image-to-image geometric error derived from the Australian scene pair comprising a Planet Labs PBC Tanager scene and a Landsat Operational Land Imager scene....18
23. Error scatterplot of image-to-image geometric error derived from the Australian scene pair comprising a Planet Labs PBC Tanager scene and a Landsat Operational Land Imager scene....18
24. Image-to-image geometric error map with error vector for each grid derived from the Chinese scene pair comprising a Planet Labs PBC Tanager scene and a Landsat Operational Land Imager scene....19
25. Histogram of image-to-image geometric error derived from the Chinese scene pair comprising a Planet Labs PBC Tanager scene and a Landsat Operational Land Imager scene....20
26. Error scatterplot of image-to-image geometric error derived from the Chinese scene pair comprising a Planet Labs PBC Tanager scene and a Landsat Operational Land Imager scene....20
27. Image-to-image geometric error map with error vector for each grid derived from the Italian scene pair comprising a Planet Labs PBC Tanager scene and a Landsat Operational Land Imager scene....21
28. Histogram of image-to-image geometric error derived from the Italian scene pair comprising a Planet Labs PBC Tanager scene and a Landsat Operational Land Imager scene....22

29. Error scatterplot of image-to-image geometric error derived from the Italian scene pair comprising a Planet Labs PBC Tanager scene and a Landsat Operational Land Imager scene....22
30. Radiometric scatterplots comparing Top of Atmosphere reflectance values derived from all seven bands of the spectrally resampled Mojave Desert, Arizona, Planet Labs PBC Tanager scene and Landsat Operational Land Imager scene....24
31. Radiometric scatterplots comparing Top of Atmosphere reflectance values derived from all seven bands of the spectrally resampled Indian Planet Labs PBC Tanager scene and Landsat Operational Land Imager scene 26
32. Radiometric scatterplots comparing Top of Atmosphere reflectance values derived from all seven bands of the spectrally resampled Sudanese Planet Labs PBC Tanager scene and Landsat Operational Land Imager scene 28
33. Radiometric scatterplots comparing Top of Atmosphere reflectance values derived from all seven bands of the spectrally resampled Australian Planet Labs PBC Tanager scene and Landsat Operational Land Imager scene 30
34. Radiometric scatterplots comparing Top of Atmosphere reflectance values derived from all seven bands of the spectrally resampled Chinese Planet Labs PBC Tanager scene and Landsat Operational Land Imager scene 32
35. Radiometric scatterplots comparing Top of Atmosphere reflectance values derived from all seven bands of the spectrally resampled Italian Planet Labs PBC Tanager scene and Landsat Operational Land Imager scene 34
36. Image of Railroad Valley, Nevada, Planet Labs PBC Tanager scene from April 19, 2025, and a graph comparing the Top of Atmosphere reflectance of the Tanager scene and the Radiometric Calibration Network dataset RVUS_2025_109....37
37. Image of Railroad Valley, Nevada, Planet Labs PBC Tanager scene from May 10, 2025, and a graph showing comparing the Top of Atmosphere reflectance of the Tanager scene and the Radiometric Calibration Network dataset RVUS_2025_130....38
38. Plot showing the spectral shift analysis results derived from a Railroad Valley, Nevada, Planet Labs PBC Tanager scene along the upper scanline 39
39. Plot showing the spectral shift analysis results derived from a Railroad Valley, Nevada, Planet Labs PBC Tanager scene along the lower scanline....40
40. Image of Lyndon B. Johnson Causeway, Texas, Planet Labs PBC Tanager scene....41
41. Graph of root mean square difference curves and corresponding minimum full width at half maximum lines for all bands derived from the Lyndon B. Johnson Causeway, Texas, Planet Labs PBC Tanager scene....41
42. Graph of full width at half maximum for all bands derived from the Lyndon B. Johnson Causeway, Texas, Planet Labs PBC Tanager scene 42
43. Image of St. Louis Bay Bridge, Mississippi, Planet Labs PBC Tanager scene....42
44. Root mean square difference curves and corresponding minimum full width at half maximum lines for all bands derived from the St. Louis Bay Bridge, Mississippi, Planet Labs PBC Tanager scene....42
45. Full width at half maximum for all bands derived from the St. Louis Bay Bridge, Mississippi, Planet Labs PBC Tanager scene....43
46. Graphs showing point spread function with full width at half maximum in red line, modulation transfer function with Nyquist frequency marked with a vertical dashed line, relative edge response with lower and upper bound of the central one pixel marked with dashed lines, and modulation transfer function in full range with Nyquist frequency marked with a vertical dashed line....44

Tables

1. Satellite and operational details for the Planet Labs PBC Tanager 2
2. Imaging sensor details for the Planet Labs PBC Tanager 2
3. U.S. Geological Survey measurement results for the Planet Labs PBC Tanager 3
4. Summary of band-to-band scene results using band 38 as a reference 3
5. Geometric error of the Planet Labs PBC Tanager relative to Landsat Operational Land Imager 10
6. Top of Atmosphere reflectance comparison of the Planet Labs PBC Tanager and Landsat Operational Land Imager 23
7. Spatial performance of the Planet Labs PBC Tanager over the Lyndon B. Johnson Causeway, Texas, and the St. Louis Bay Bridge, Mississippi 43

Conversion Factors

International System of Units to U.S. customary units

Multiply	By	To obtain
	Length	
nanometer (nm)	3.93701×10^{-8}	inch (in.)
micrometer (µm)	3.9370×10^{-5}	inch (in.)
meter (m)	3.281	foot (ft)
meter (m)	1.094	yard (yd)
kilometer (km)	0.6214	mile (mi)

Abbreviations

ECCOE	Earth Resources Observation and Science Cal/Val Center of Excellence
FWHM	full width at half maximum
GSD	ground sample distance
JACIE	Joint Agency Commercial Imagery Evaluation
OLI	Operational Land Imager
RadCalNet	Radiometric Calibration Network
RMSD	root mean square difference
TOAR	Top of Atmosphere reflectance
USGS	U.S. Geological Survey

System Characterization Report on Tanager

By Minsu Kim,[1] Seonkyung Park,[2] Cody Anderson,[3] Jeff Clauson,[3] Jim Vrabel,[1] and Ajit Sampath[1]

Executive Summary

This report addresses the system characterization of the Tanager satellite hyperspectral sensor created by Planet Labs PBC and is part of a series of system characterization reports produced and delivered by the U.S. Geological Survey Earth Resources Observation and Science Cal/Val Center of Excellence. These reports present and detail the methodology and procedures for characterization; present technical and operational information about the Tanager hyperspectral sensor; and provide a summary of test measurements, data retention practices, data analysis results, and conclusions.

This report summarizes the sensor performance of the Tanager based on the U.S. Geological Survey Earth Resources Observation and Science Cal/Val Center of Excellence system characterization process. In summary, we determined that the Tanager exhibits a band-to-band geometric error ranging from −0.074 to 0.097 pixel. Compared to the Landsat Operational Land Imager, geometric offsets ranged from −5.980 meters (−0.20 pixel) to 11.348 meters (0.40 pixel). Radiometric comparisons showed offsets between −0.004 and 0.056 with slopes from 0.830 to 1.066. Spectral shifts are found between 0.65 and 0.75 nanometers. Finally, spatial performance evaluation yielded a point spread function full width at half maximum of 1.27 to 1.75 pixels, a relative edge response of 0.802 to 0.651, and a modulation transfer function at Nyquist of 0.488 to 0.253.

Introduction

This report addresses the system characterization of the Tanager satellite hyperspectral sensor created by Planet Labs PBC and is part of a series of system characterization reports produced and delivered by the U.S. Geological Survey (USGS) Earth Resources Observation and Science Cal/Val Center of Excellence. These reports present and detail the methodology and procedures for characterization; present technical and operational information about the Tanager hyperspectral sensor; and provide a summary of test measurements, data retention practices, data analysis results, and conclusions.

The Planet Labs PBC Tanager is a hyperspectral electro-optical instrumentation designed to deliver imagery across the visible and shortwave infrared regions. The Tanager supports a broad spectrum of applications, but its core mission is to detect and mitigate methane emissions across the globe. The Tanager is able to map facility-scale methane emissions to enhance leak detection and repair efforts (Planet Labs PBC, 2026).

The data analysis results provided within this report have been derived from approved Joint Agency Commercial Imagery Evaluation (JACIE) processes and procedures (Cantrell and Christopherson, 2024). The JACIE was formed to leverage resources from several Federal agencies for the characterization of remote sensing data and to share those results across the remote sensing community. More information about JACIE is available at https://www.usgs.gov/calval/jacie.

The purpose of this report is to describe the Tanager hyperspectral sensor, test its performance in B2B, I2I, radiometric, and spatial, complete related data analyses to quantify these performances, and report the results in a standardized document. In this chapter, the Tanager hyperspectral sensor is described. The performance testing of the system involved geometric, radiometric, and spatial analyses. The scope of the geometric analysis is limited to testing the interior alignments of spectral bands against each other, and the exterior alignment is tested in reference to the Landsat Operational Land Imager (OLI; U.S. Geological Survey, 2025).

The USGS Earth Resources Observation and Science Cal/Val Center of Excellence (ECCOE; U.S. Geological Survey, 2020) and the associated system characterization process used for this assessment follow the USGS Fundamental Science Practices, which include maintaining data, information, and documentation needed to reproduce and validate the scientific analysis documented in this report. Additional information and guidance about Fundamental Science Practices and related resource information of interest to the public are available at https://www.usgs.gov/about/organization/science-support/office-science-quality-and-integrity/fundamental-science-practices. For additional information related to the report, please contact ECCOE at eccoe@usgs.gov.

[1]KBR, Inc., under contract to the U.S. Geological Survey.

[2]USS, Inc., under contract to the U.S. Geological Survey.

[3]U.S. Geological Survey.

System Description

This section describes the satellite and operational details and provides information about the Planet Labs PBC Tanager hyperspectral sensor. Hyperspectral data provide finer spectral signatures to be used for scientific analysis.

Satellite and Operational Details

The satellite and operational details for Tanager are listed in table 1.

Sensor Information

The imaging sensor details for Tanager are listed in table 2. The spectral resolution of each band is 5 nanometers (nm) for full width at half maximum (FWHM).

Table 1. Satellite and operational details for the Planet Labs PBC Tanager (Planet Labs PBC, 2026).

[km, kilometer; °, degree; ±, plus or minus; m, meter]

Product information	Tanager
Satellite and operational information	
Sensor name(s)	Tanager-1 (Carbon Mapper-1 platform alias)
Sensor type	Hyperspectral
Mission type	Global methane detection and land-monitoring mission
Launch date	August 16, 2024
Expected lifetime	5 years
Operational details	
Operating orbit	Sun-synchronous orbit
Orbital altitude range	510 km
Sensor angle altitude	97.4° inclination
Imaging time	11:00 a.m. (local time)
Geographic coverage	18-km swath
Temporal resolution	7 days
Temporal coverage	2024 to present (2026)
Imaging angles	±30°
Ground sample distance(s)	30–35 m
Product abstract	https://docs.planet.com/data/imagery/tanager/

Table 2. Imaging sensor details for the Planet Labs PBC Tanager (Planet Labs PBC, 2026).

[µm, micrometer; GSD, ground sample distance; m, meter; VNIR, visible and near infrared; ~, about; SWIR, shortwave infrared]

Spectral band details	Tanager			
	Lower band (µm)	Upper band (µm)	Radiometric resolution (bits)	GSD (m)
VNIR (~204 bands)	0.700	1.400	32	30.0–35.0
SWIR (220 bands)	1.400	2.500	32	30.0–35.0

Procedures

The ECCOE has established standard processes to identify Earth observing systems of interest and to assess the geometric and radiometric qualities of data products from these systems (Cantrell and Christopherson, 2024).

The assessment steps are as follows:

1. System identification and investigation to learn the general specifications of the satellite and its sensor(s);
2. Data receipt and initial inspection to understand the characteristics and any overt flaws in the data product so that it may be further analyzed;
3. Geometric characterization, including interior geometric orientation measuring the relative alignment of spectral bands and exterior geometric orientation measuring how well the georeferenced pixels within the image are aligned to a known reference; and
4. Radiometric characterization, including assessing how well the data product correlates with a known reference and, when possible, assessing the signal-to-noise ratio.

The specific procedures required to handle hyperspectral data are as follows:

- Correction of defective pixels that cause dark striping;
- Spectral resampling of hyperspectral data to match the spectral response function of Landsat OLI; and
- Computation of solar irradiance by resampling high-resolution extraterrestrial solar irradiance based on the spectral response function of Landsat OLI.

Data analysis and test results are maintained at the USGS Earth Resources Observation and Science Center by the ECCOE project.

Measurements

The observed USGS measurements are listed in table 3. Details about the methodologies used are outlined in the "Analysis" section.

Analysis

This section of the report describes the geometric and radiometric performance of the Tanager hyperspectral sensor.

Geometric Performance

The geometric performance for the Tanager sensor is characterized in terms of the band-to-band alignment and image-to-image relative geometric accuracy.

Band to Band

For this analysis, each band of the Tanager imagery was registered against one reference band (band 38 at 561 nm). Scene identifiers for all band-to-band scenes discussed in this report are provided in table 4. Scene identifier

Table 3. U.S. Geological Survey measurement results for the Planet Labs PBC Tanager.

[nm, nanometer; RMSE, root mean square error; OLI, Operational Land Imager; m, meter; R^2, coefficient of determination; %, percent; RER, relative edge response; FWHM, full width at half maximum; MTF, modulation transfer function]

Description of product	System characterization results
Geometric performance (easting, northing), in meters (pixels)	
Band to band (561-nm reference, band 38)	Mean: −0.071 to 0.068 pixel, −0.074 to 0.097 pixel RMSE: 0.201 to 0.506 pixel, 0.202 to 0.479 pixel
Image to image (against OLI)	Easting mean: −5.980 to 4.168 m (−0.20 to 0.14 pixel) Easting RMSE: 6.517 to 11.948 m (0.22 to 0.40 pixel) Northing mean: −3.031 to 5.167 m (−0.10 to 0.17 pixel) Northing RMSE: 6.101 to 11.101 m (0.20 to 0.37 pixel)
Radiometric performance (offset, slope, R^2, uncertainty [%])	
Radiometric evaluation (linear regression—Tanager versus OLI reflectance)	Band 1: −0.006 to 0.013, 0.922 to 1.065, 0.870 to 0.982, 2.56 to 6.36 Band 2: −0.006 to 0.010, 0.932 to 1.076, 0.880 to 0.981, 2.81 to 8.21 Band 3: 0.003 to 0.014, 0.906 to 1.052, 0.870 to 0.985, 4.31 to 11.22 Band 4: 0.006 to 0.023, 0.879 to 0.998, 0.886 to 0.986, 3.49 to 12.58 Band 5: 0.004 to 0.056, 0.830 to 0.991, 0.829 to 0.986, 3.22 to 6.83 Band 6: 0.005 to 0.045, 0.834 to 0.964, 0.870 to 0.983, 2.55 to 9.12 Band 7: 0.001 to 0.027, 0.874 to 0.955, 0.887 to 0.984, 2.60 to 14.25
Spectral shift	
Wavelength shift measured from the nominal band center using the oxygen A-band	0.65 to 0.75 nm
Spatial performance	
Spatial performance measurement (from long to short wavelength)	RER: 0.902 to 0.651 FWHM: 1.27 to 1.74 pixels MTF at Nyquist: 0.488 to 0.253

Table 4. Summary of band-to-band scene results using band 38 as a reference (in pixels).

[ID, identifier; RMSE, root mean square error]

Scene location	Tanager scene ID	Mean error (easting)	Mean error (northing)	RMSE (easting)	RMSE (northing)
Mojave Desert, Arizona	20250405_190836_16_4001	−0.071 to 0.068	−0.074 to 0.032	0.275 to 0.463	0.276 to 0.479
India	20250420_060625_00_4001	−0.047 to 0.051	−0.049 to 0.031	0.301 to 0.506	0.286 to 0.479
Sudan	20250502_090330_87_4001	−0.031 to 0.049	−0.012 to 0.033	0.302 to 0.452	0.274 to 0.421
Australia	20250305_010639_32_4001	−0.028 to 0.023	−0.024 to 0.030	0.201 to 0.408	0.202 to 0.398
China	20250523_055213_30_4001	−0.061 to 0.012	−0.013 to 0.097	0.241 to 0.282	0.259 to 0.312

20250405_190836_16_4001 shows part of the Mojave Desert in Arizona and was used as an example image to compute band-to-band error. The grid system and error vectors for band 22 are shown in figure 1. The red arrows show the relative error vector for each yellow grid, with x and y vector components representing the easting and northing error, respectively. Grids with missing arrows represent the outliers. Also, the scatterplot of the easting-northing error shows a distribution with three circles representing one, two, and three standard deviations.

For the Mojave Desert scene, the mean difference and root mean square error values for the easting direction are shown in figure 2, and those values for the northing direction are shown in figure 3. Similarly, figures 4 and 5 are band-to-band results for the Indian Tanager scene (20250420_060625_00_4001). The band-to-band results for the Sudanese Tanager scene (20250502_090330_87_4001) are shown in figures 6 and 7. The band-to-band results for the Australian Tanager scene (20250305_010639_32_4001) are shown in figures 8 and 9. The band-to-band results for the Chinese Tanager scene (20250523_055213_30_4001) are shown in figures 10 and 11. The band-to-band results of all five scenes are summarized in table 4, where the erroneous values near the water vapor bands were not included in the result range summary in table 4.

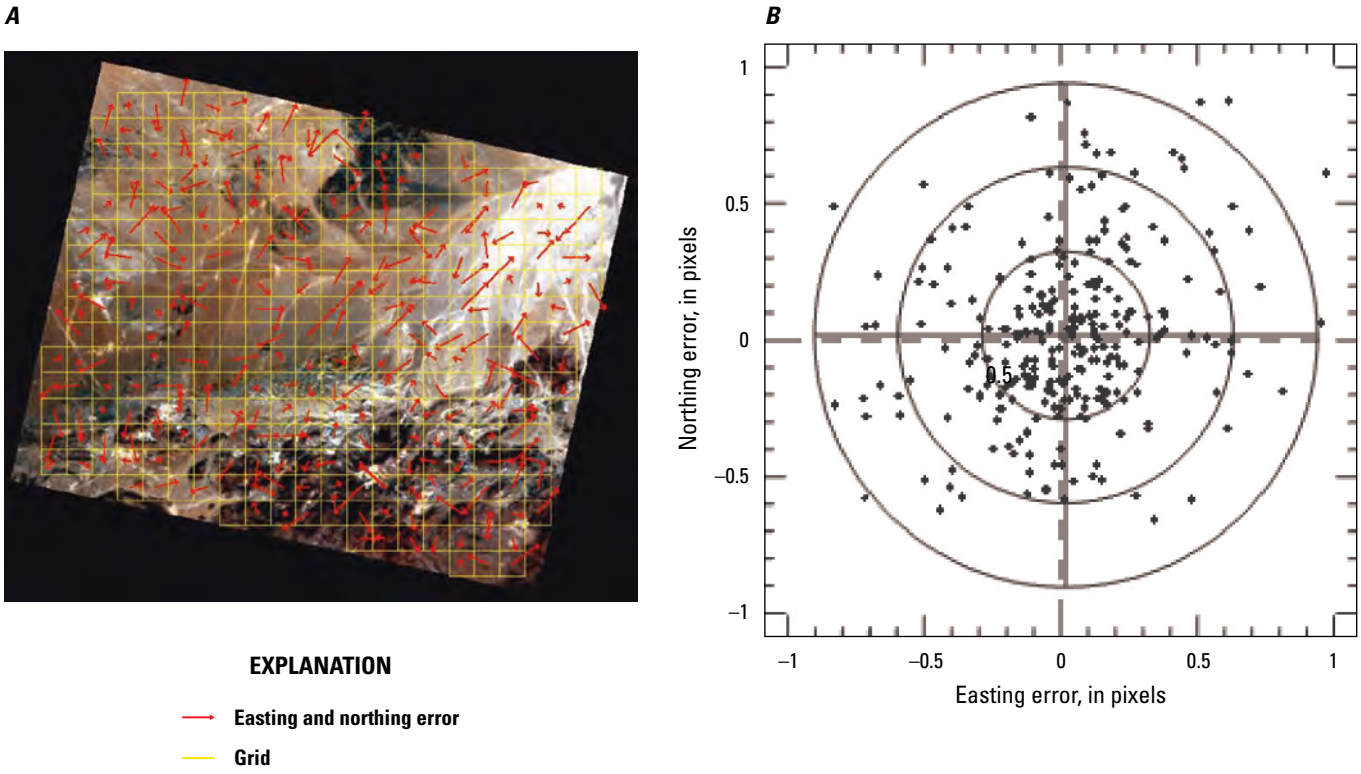

Figure 1. The Mojave Desert, Arizona, Planet Labs PBC Tanager scene (20250405_190836_16_4001) used to compute band-to-band error. *A*, image of grid showing band-to-band geometric error map of band 22 (481 nanometers) using band 38 (561 nanometers) as reference; *B*, the error vector scatterplot. Image copyrighted by Planet Labs PBC, licensed under the Creative Commons Attribution-NonCommercial-ShareAlike 2.0 Generic license.

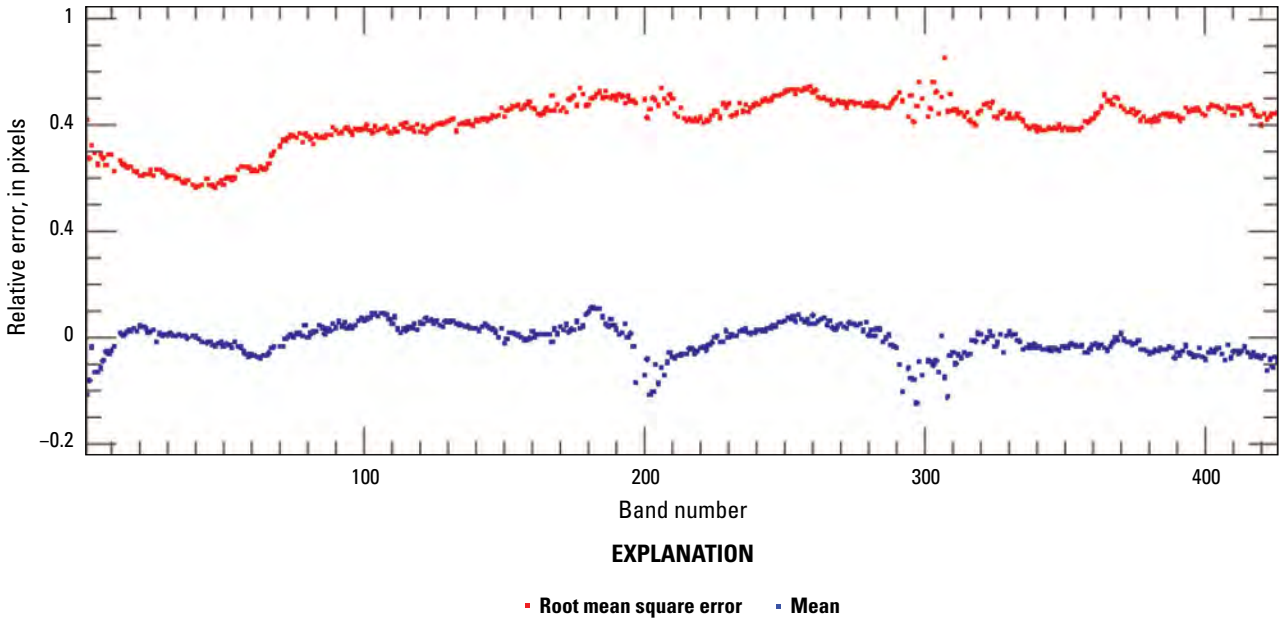

Figure 2. Graph showing relative band-to-band easting geometric error derived from the Mojave Desert, Arizona, Planet Labs PBC Tanager scene (20250405_190836_16_4001) using band 38 as a reference.

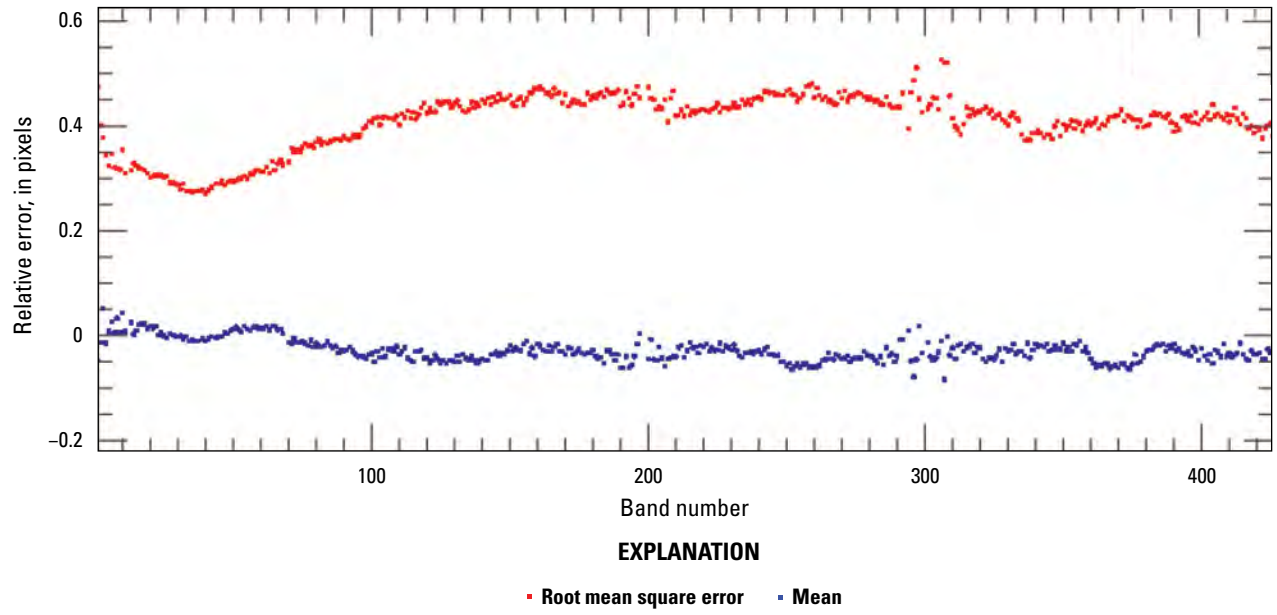

Figure 3. Graph showing relative band-to-band northing geometric error derived from the Mojave Desert, Arizona, Planet Labs PBC Tanager scene (20250405_190836_16_4001) using band 38 as a reference.

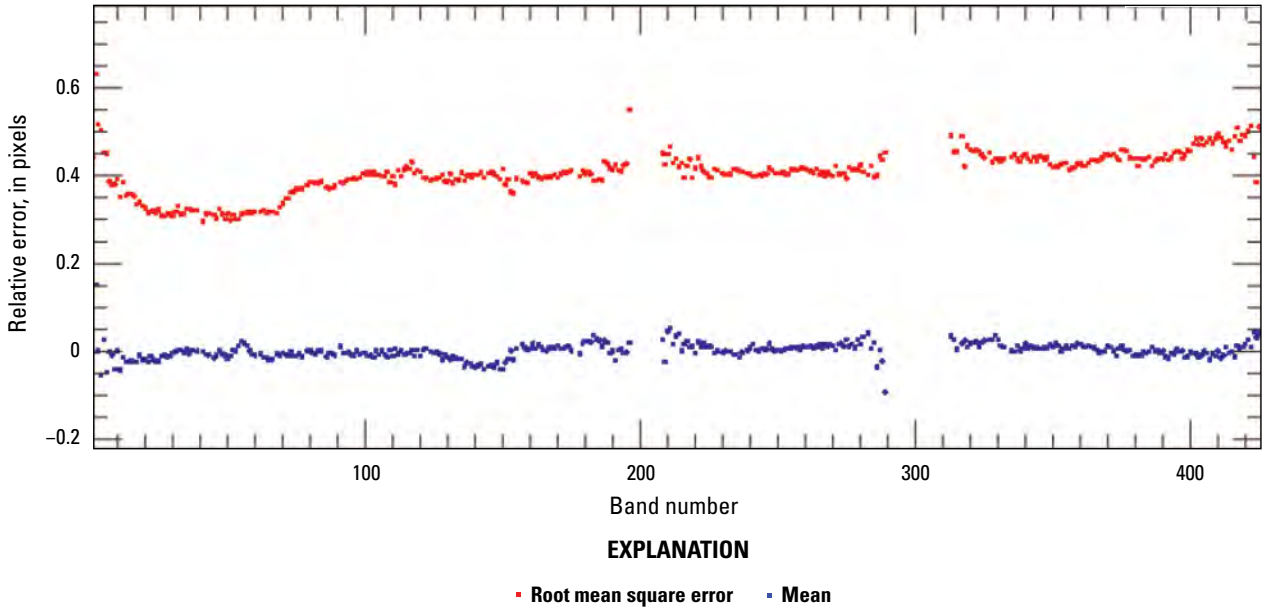

Figure 4. Graph showing relative band-to-band easting geometric error derived from the Indian Planet Labs PBC Tanager scene (20250420_060625_00_4001) using band 38 as a reference.

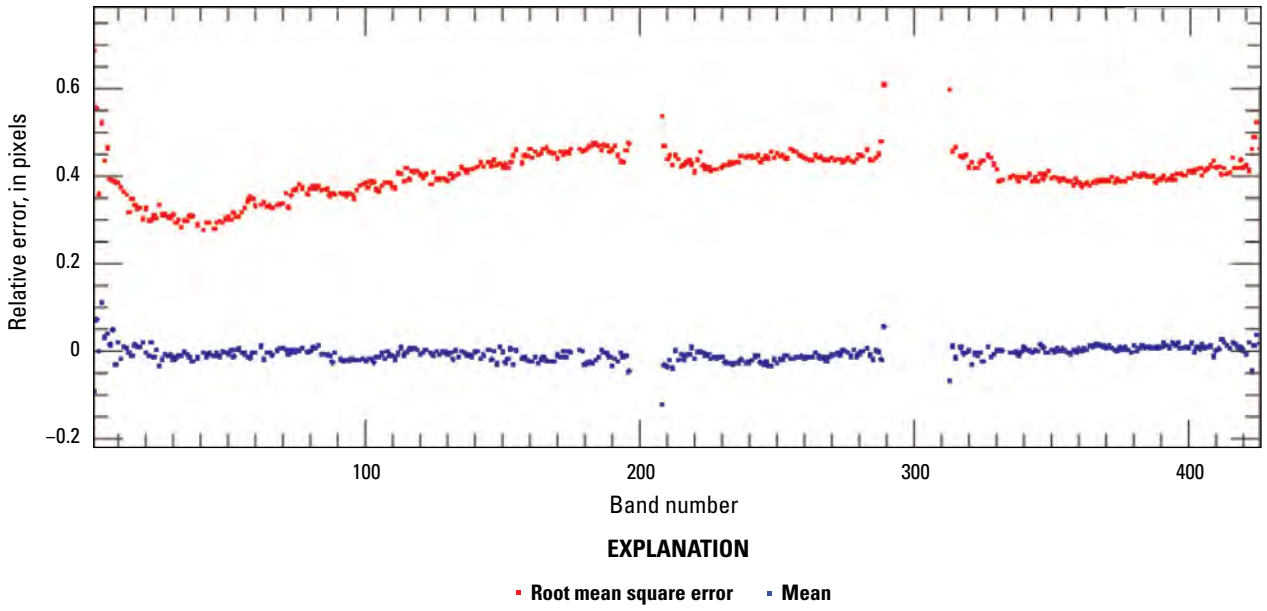

Figure 5. Graph showing relative band-to-band northing geometric error derived from the Indian Planet Labs PBC Tanager scene (20250420_060625_00_4001) using band 38 as a reference.

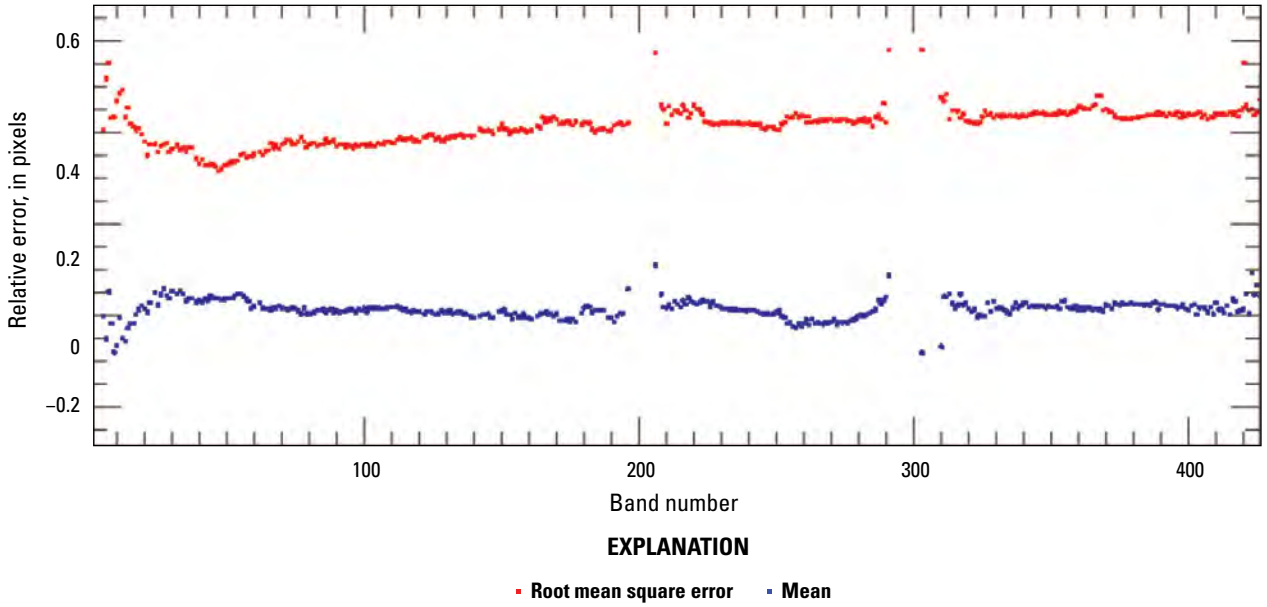

Figure 6. Graph showing relative band-to-band easting geometric error derived from the Sudanese Planet Labs PBC Tanager scene (20250502_090330_87_4001) using band 38 as a reference.

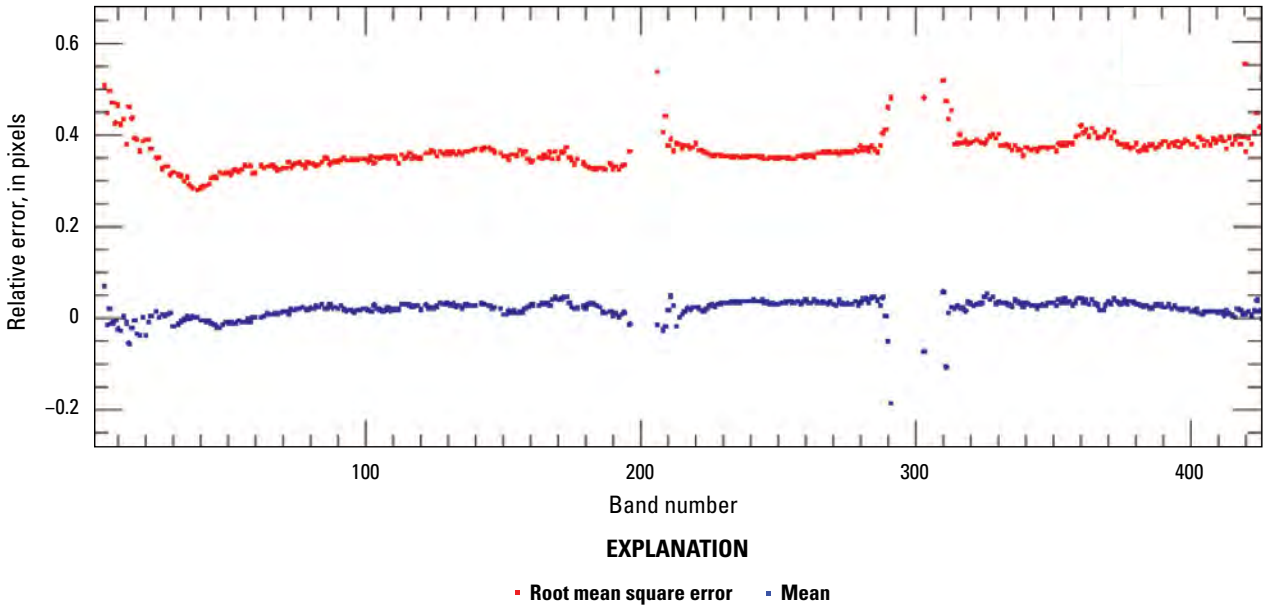

Figure 7. Graph showing relative band-to-band northing geometric error derived from the Sudanese Planet Labs PBC Tanager scene (20250502_090330_87_4001) using band 38 as a reference.

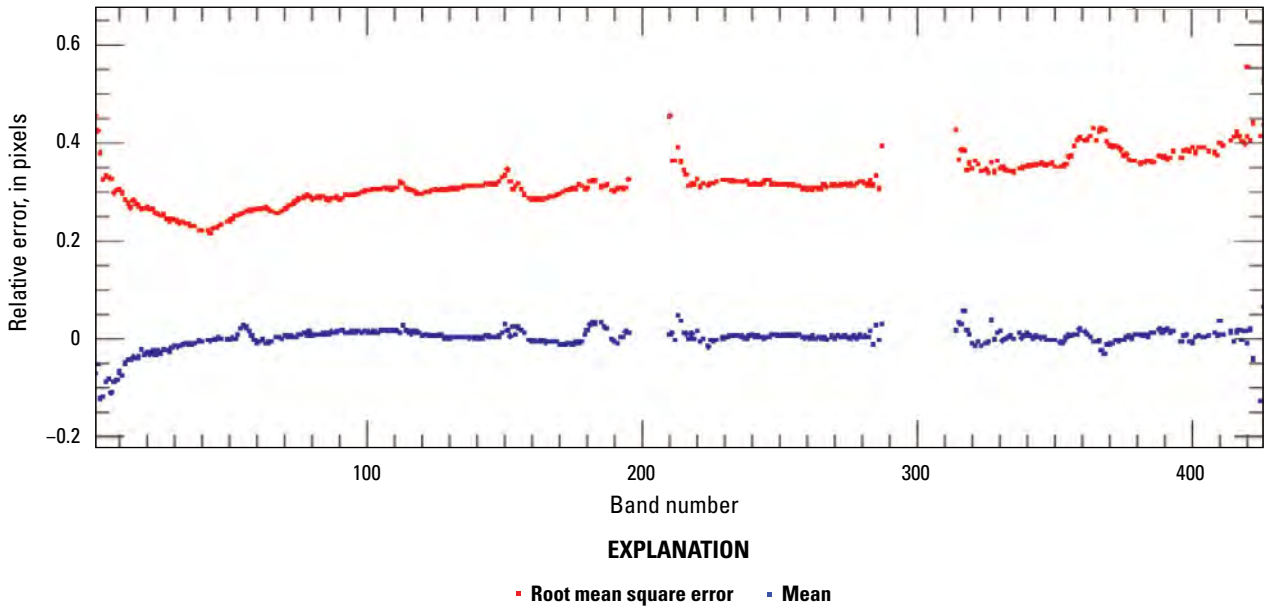

Figure 8. Graph showing relative band-to-band easting geometric error derived from the Australian Planet Labs PBC Tanager scene (20250305_010639_32_4001) using band 38 as a reference.

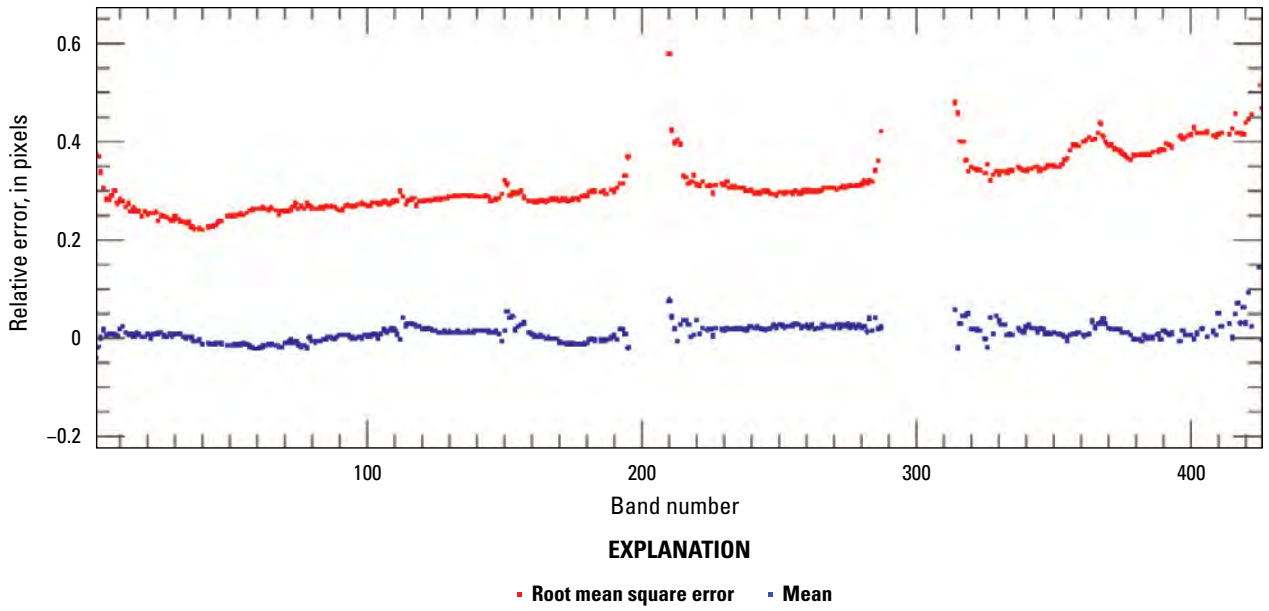

Figure 9. Graph showing relative band-to-band northing geometric error derived from the Australian Planet Labs PBC Tanager scene (20250305_010639_32_4001) using band 38 as a reference.

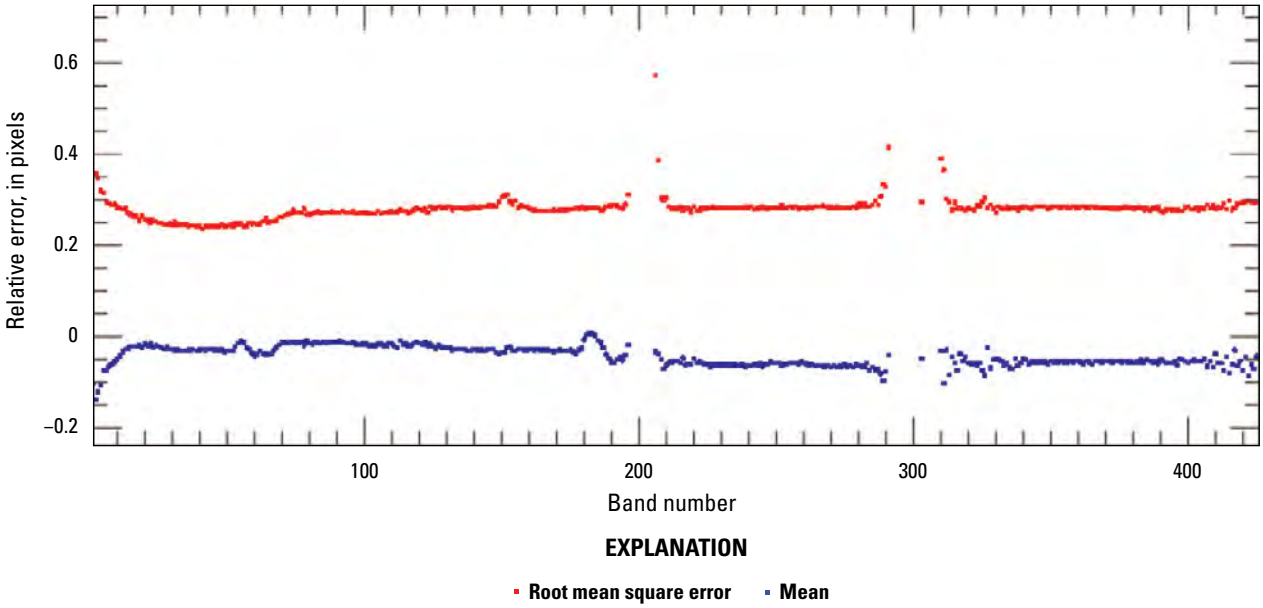

Figure 10. Graph showing relative band-to-band easting geometric error derived from the Chinese Planet Labs PBC Tanager scene (20250523_055213_30_4001) using band 38 as a reference.

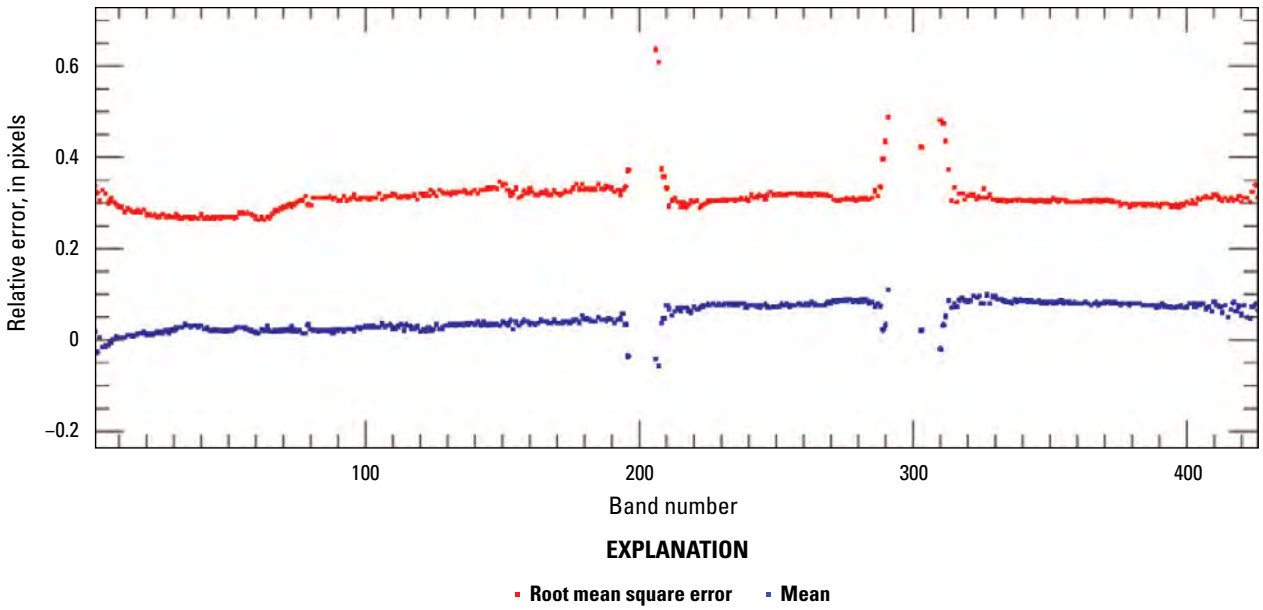

Figure 11. Graph showing relative band-to-band northing geometric error derived from the Chinese Planet Labs PBC Tanager scene (20250523_055213_30_4001) using band 38 as a reference.

Image to Image

For this analysis, spectrally resampled Tanager reflectance (ρ_i), where the subscript i represents the i-th Landsat OLI band, was used. The spectral resampling of Tanager hyperspectral reflectance, $\rho_{Tanager}(\lambda)$, where λ denotes wavelength, is performed using the Landsat OLI spectral response function, $\Re_{OLI\_i}(\lambda)$ (Barsi and others, 2014).

$$\rho_i = \frac{\int \rho_{Tanager}(\lambda)\Re_{OLI\_i}(\lambda)\mathrm{d}\lambda}{\int \Re_{OLI\_i}(\lambda)\mathrm{d}\lambda}. \quad (1)$$

Six Tanager-Landsat OLI scene pairs were used for image-to-image analysis. A normalized cross-correlation matrix was computed, and its local maxima with subpixel analysis were determined to estimate the mean error and root mean square error results shown in table 5 and represented in pixels at a 30-meter (m) ground sample distance (GSD).

For each of the six Tanager images, geometric error maps illustrating the directional shift and relative magnitude of the shift, when compared with Landsat OLI, are provided in figures 12 through 29.

Radiometric Performance

For this analysis, cloud-free regions of interest were selected within three near-coincident Tanager-Landsat OLI scene pairs. Top of Atmosphere reflectance (TOAR) comparison results are listed in table 6.

Once the relative georeferencing error between the Landsat OLI and Tanager has been corrected, TOAR values from the two sensors are extracted. The scatterplots shown in figures 30 through 35 are drawn in a way that the x-axis is the reference sensor (Landsat OLI) and the y-axis is the comparison sensor (Tanager). Ideally, the slope should be near unity (1.0) because it is spectrally resampled from hyperspectral data using spectral response of Landsat OLI, and the offset should be near zero. If the slope is greater than unity, that means Tanager tends to overestimate TOAR compared to Landsat OLI. A band-by-band graphical comparison of the Mojave Desert, Indian, Sudanese, Australian, Chinese, and Italian Tanager-Landsat OLI scene pairs is shown in figures 30 through 35.

Table 5. Geometric error of the Planet Labs PBC Tanager relative to Landsat Operational Land Imager.

[OLI, Operational Land Imager; ID, identifier; RMSE, root mean square error; m, meter]

Scene location	Tanager scene ID	Landsat OLI scene ID	Mean error (easting)	Mean error (northing)	RMSE (easting)	RMSE (northing)
Mojave Desert, Arizona	20250405_190836_16_4001	LC08_L1TP_040035_20250405_20250412_02_T1	3.016 m (0.10 pixel)	5.167 m (0.17 pixel)	8.605 m (0.29 pixel)	10.935 m (0.36 pixel)
India	20250420_060625_00_4001	LC09_L1TP_146043_20250420_20250420_02_T1	1.167 m (0.04 pixel)	4.477 m (0.15 pixel)	11.948 m (0.40 pixel)	11.101 m (0.37 pixel)
Sudan	20250502_090330_87_4001	LC08_L1TP_174049_20250502_20250508_02_T1	−5.980 m (−0.20 pixel)	−0.280 m (−0.01 pixel)	11.430 m (0.38 pixel)	11.068 m (0.37 pixel)
Australia	20250305_010639_32_4001	LC09_L1TP_096076_20250305_20250305_02_T1	−0.103 m (−0.00 pixel)	−3.031 m (−0.10 pixel)	6.616 m (0.22 pixel)	6.920 m (0.23 pixel)
China	20250523_055213_30_4001	LC08_L1TP_145028_20250523_20250602_02_T1	4.168 m (0.14 pixel)	0.102 m (0.00 pixel)	8.389 m (0.28 pixel)	10.387 m (0.35 pixel)
Italy	20250627_103759_58_4001	LC09_L1TP_190031_20250627_20250627_02_T1	−3.231 m (−0.11 pixel)	0.439 m (0.01 pixel)	6.517 m (0.21 pixel)	6.101 m (0.20 pixel)

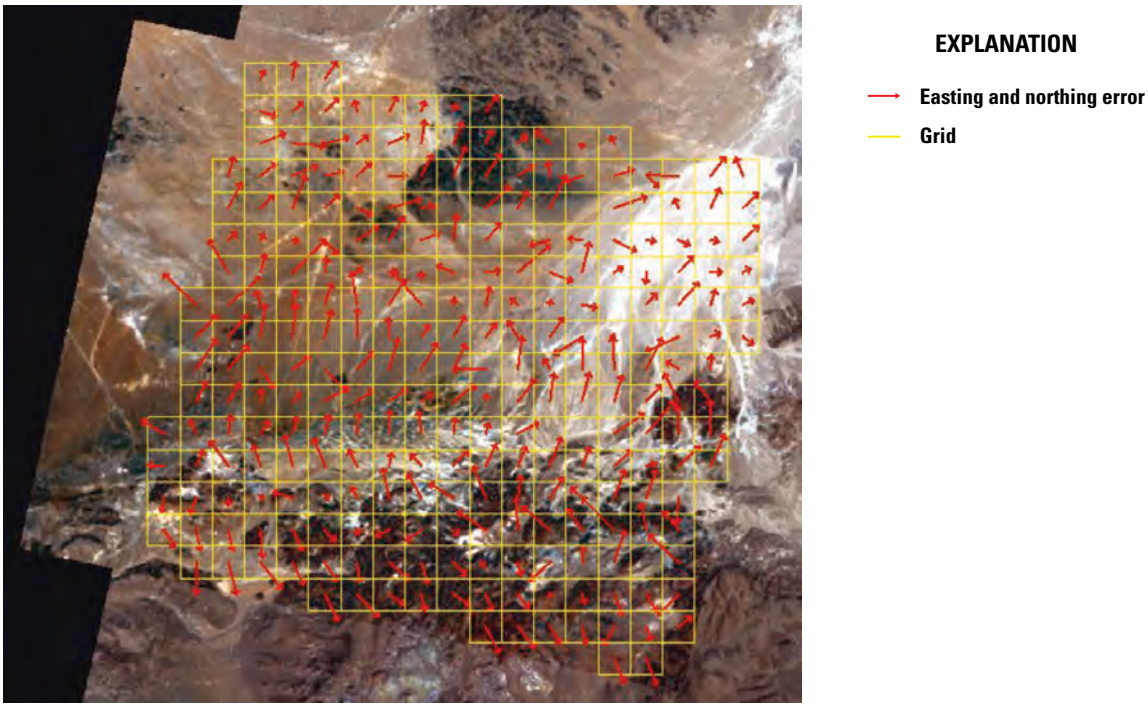

Figure 12. Image-to-image geometric error map with error vector for each grid using the Mojave Desert, Arizona, scene pair comprising a Planet Labs PBC Tanager scene (20250405_190836_16_4001) and a Landsat Operational Land Imager scene (LC08_L1TP_040035_20250405_20250412_02_T1). Tanager image copyrighted by Planet Labs PBC, licensed under the Creative Commons Attribution-NonCommercial-ShareAlike 2.0 Generic license. Landsat image by U.S. Geological Survey.

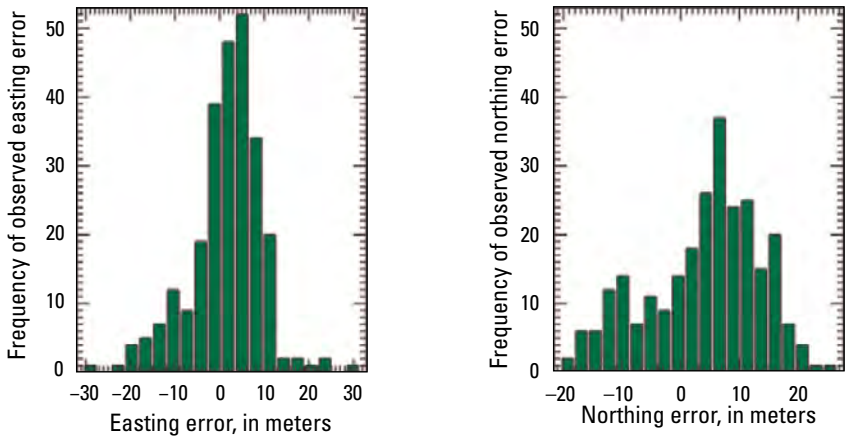

Figure 13. Histogram of image-to-image geometric error derived from the Mojave Desert, Arizona, scene pair comprising a Planet Labs PBC Tanager scene (20250405_190836_16_4001) and a Landsat Operational Land Imager scene (LC08_L1TP_040035_20250405_20250412_02_T1).

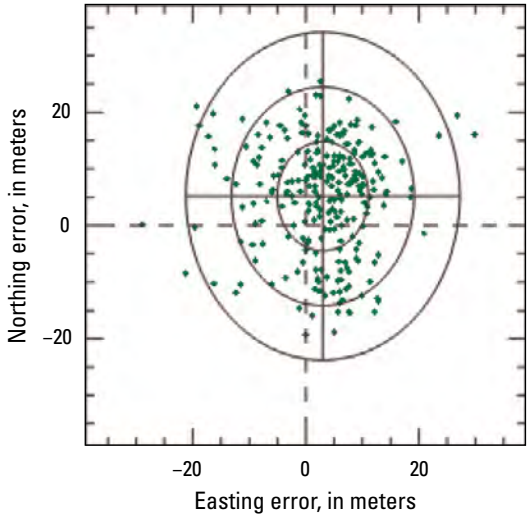

Figure 14. Error scatterplot of image-to-image geometric error derived from the Mojave Desert, Arizona, scene pair comprising a Planet Labs PBC Tanager scene (20250405_190836_16_4001) and a Landsat Operational Land Imager scene (LC08_L1TP_040035_20250405_20250412_02_T1).

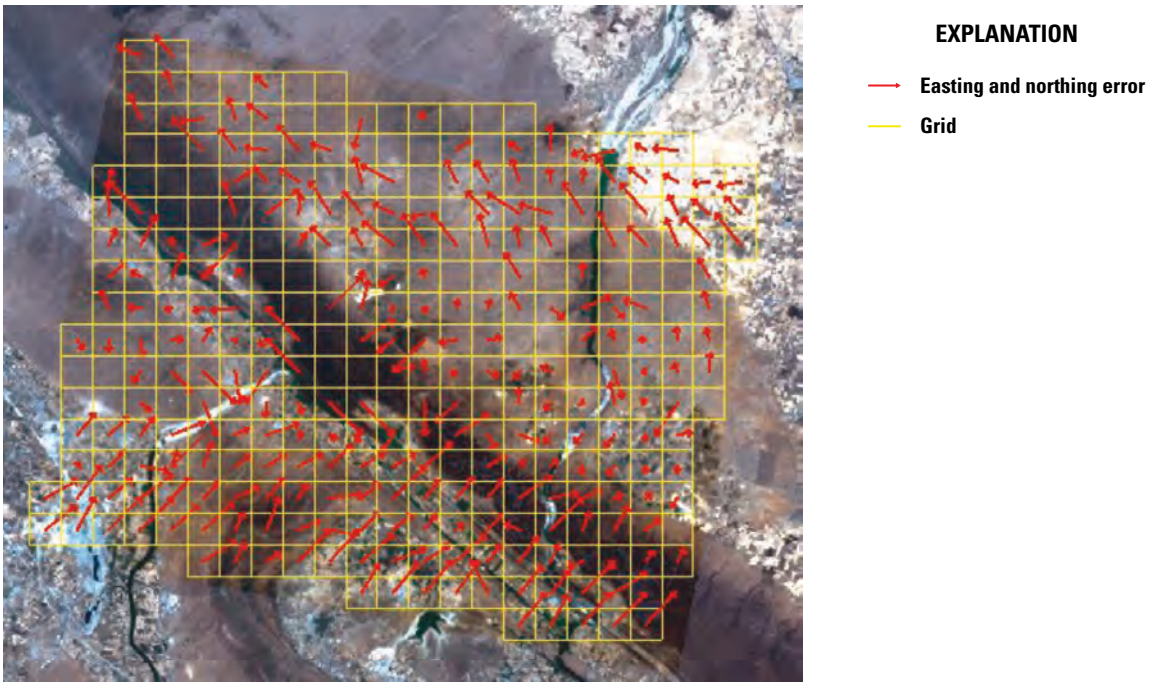

Figure 15. Image-to-image geometric error map with error vector for each grid derived from the Indian scene pair comprising a Planet Labs PBC Tanager scene (20250420_060625_00_4001) and a Landsat Operational Land Imager scene (LC09_L1TP_146043_20250420_20250420_02_T1). Tanager image copyrighted by Planet Labs PBC, licensed under the Creative Commons Attribution-NonCommercial-ShareAlike 2.0 Generic license. Landsat image by U.S. Geological Survey.

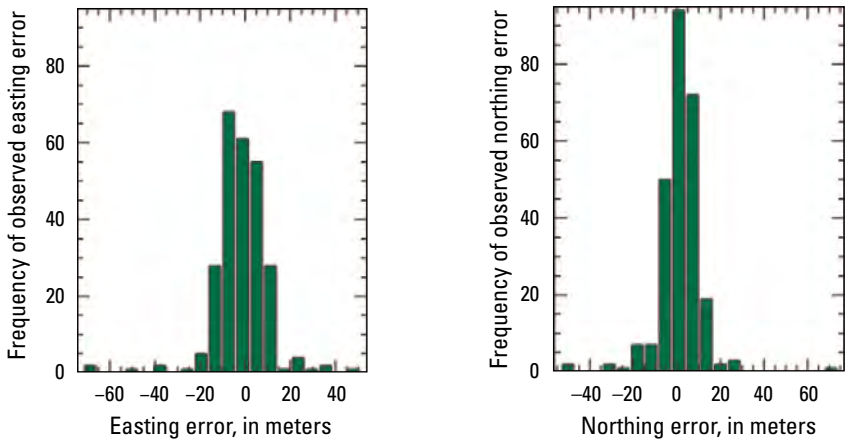

Figure 16. Histogram of image-to-image geometric derived from the Indian scene pair comprising a Planet Labs PBC Tanager scene (20250420_060625_00_4001) and a Landsat Operational Land Imager scene (LC09_L1TP_146043_20250420_20250420_02_T1).

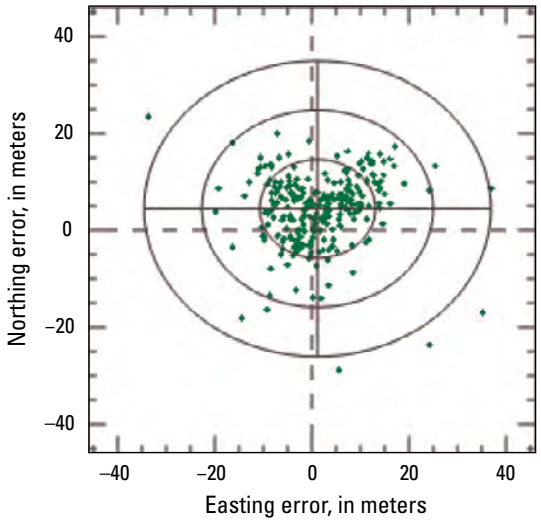

Figure 17. Error scatterplot of image-to-image geometric error derived from the Indian scene pair comprising a Planet Labs PBC Tanager scene (20250420_060625_00_4001) and a Landsat Operational Land Imager scene (LC09_L1TP_146043_20250420_20250420_02_T1).

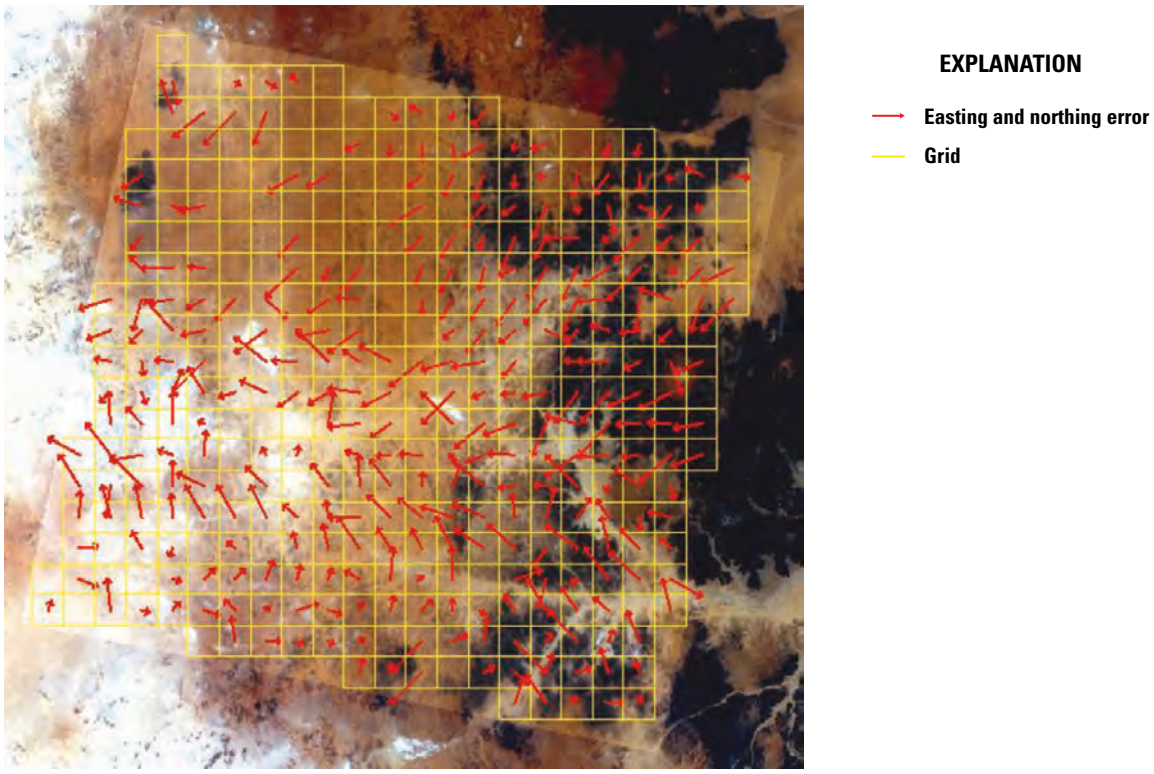

Figure 18. Image-to-image geometric error map with error vector for each grid derived from the Sudanese scene pair comprising a Planet Labs PBC Tanager scene (20250502_090330_87_4001) and a Landsat Operational Land Imager scene (LC08_L1TP_174049_20250502_20250508_02_T1). Tanager image copyrighted by Planet Labs PBC, licensed under the Creative Commons Attribution-NonCommercial-ShareAlike 2.0 Generic license. Landsat image by U.S. Geological Survey.

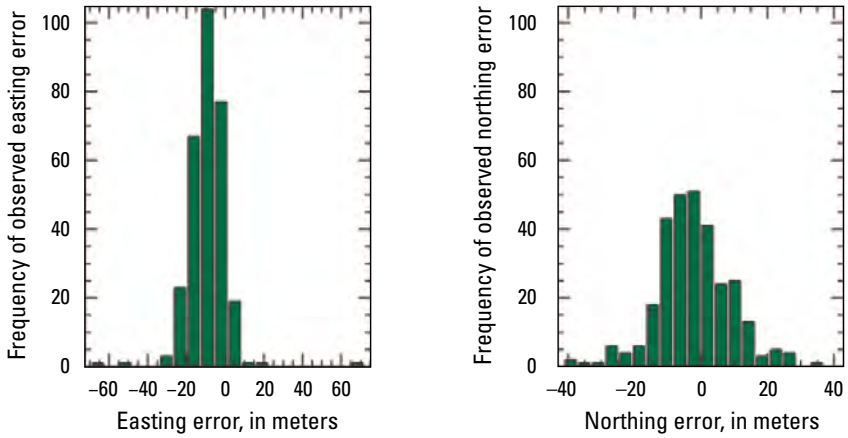

Figure 19. Histogram of image-to-image geometric error derived from the Sudanese scene pair comprising a Planet Labs PBC Tanager scene (20250502_090330_87_4001) and a Landsat Operational Land Imager scene (LC08_L1TP_174049_20250502_20250508_02_T1).

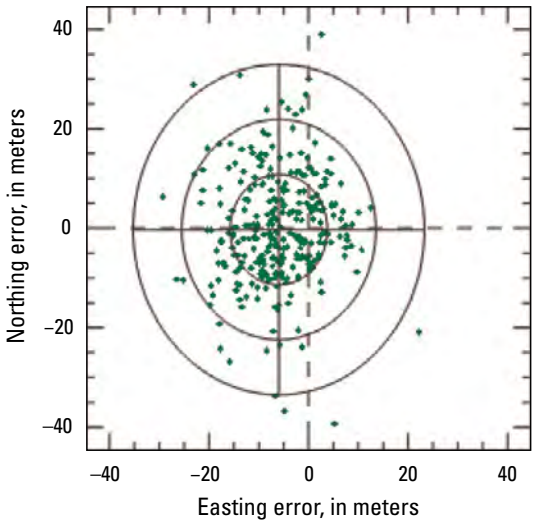

Figure 20. Error scatterplot of image-to-image geometric error derived from the Sudanese scene pair comprising a Planet Labs PBC Tanager scene (20250502_090330_87_4001) and a Landsat Operational Land Imager scene (LC08_L1TP_174049_20250502_20250508_02_T1).

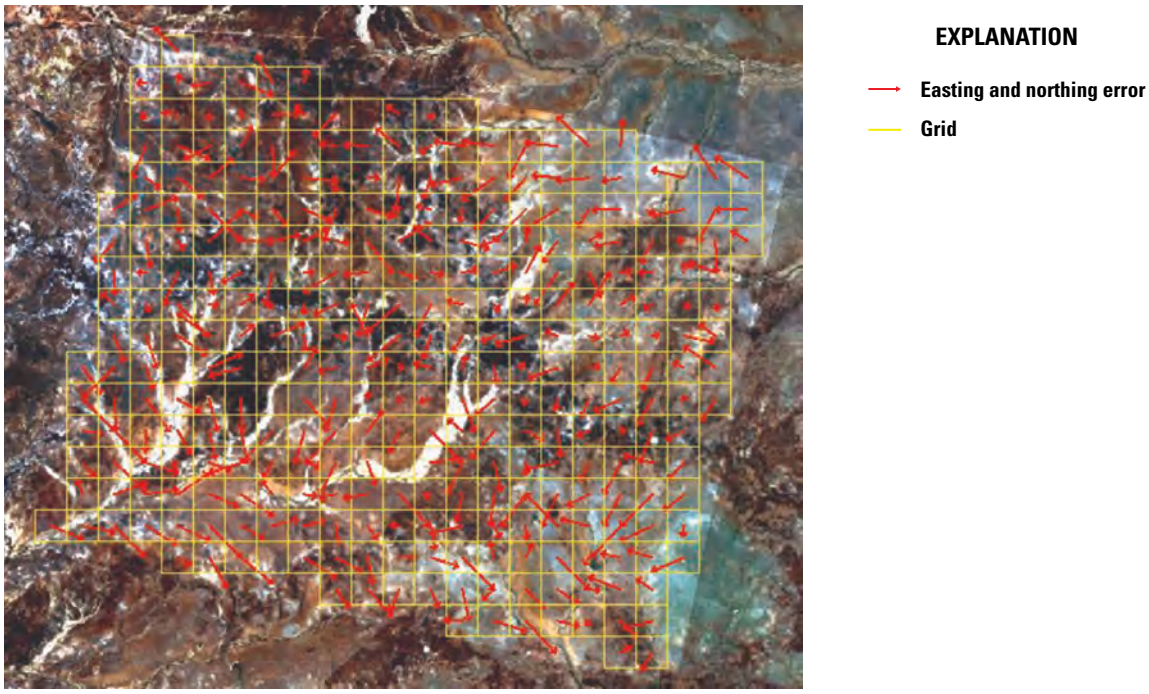

Figure 21. Image-to-image geometric error map with error vector for each grid derived from the Australian scene pair comprising a Planet Labs PBC Tanager scene (20250305_010639_32_4001) and a Landsat Operational Land Imager scene (LC09_L1TP_096076_20250305_20250305_02_T1). Tanager image copyrighted by Planet Labs PBC, licensed under the Creative Commons Attribution-NonCommercial-ShareAlike 2.0 Generic license. Landsat image by U.S. Geological Survey.

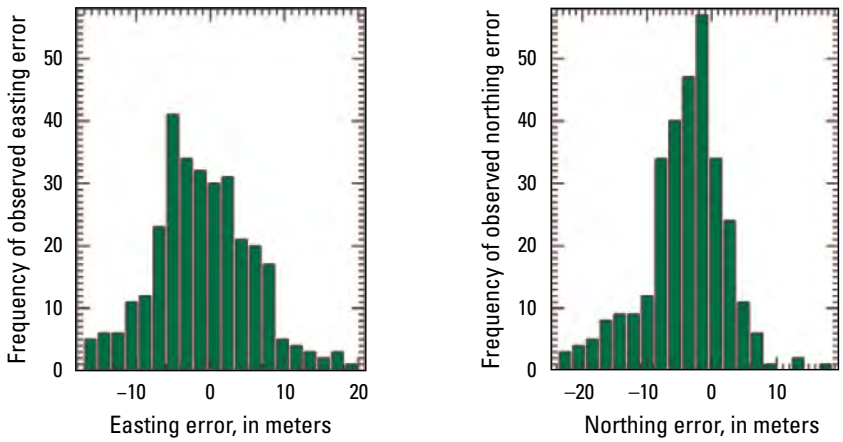

Figure 22. Histogram of image-to-image geometric error derived from the Australian scene pair comprising a Planet Labs PBC Tanager scene (20250305_010639_32_4001) and a Landsat Operational Land Imager scene (LC09_L1TP_096076_20250305_20250305_02_T1).

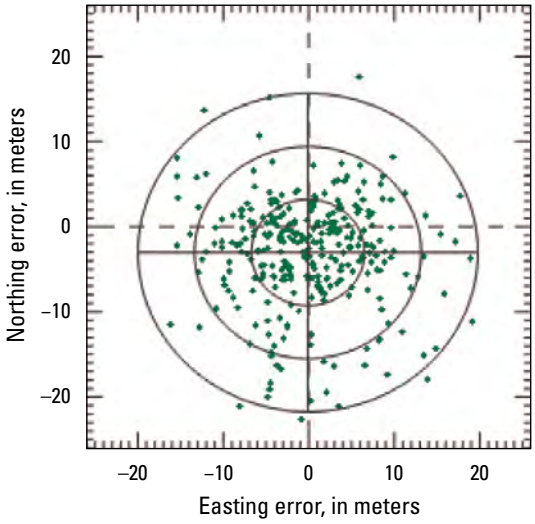

Figure 23. Error scatterplot of image-to-image geometric error derived from the Australian scene pair comprising a Planet Labs PBC Tanager scene (20250305_010639_32_4001) and a Landsat Operational Land Imager scene (LC09_L1TP_096076_20250305_20250305_02_T1).

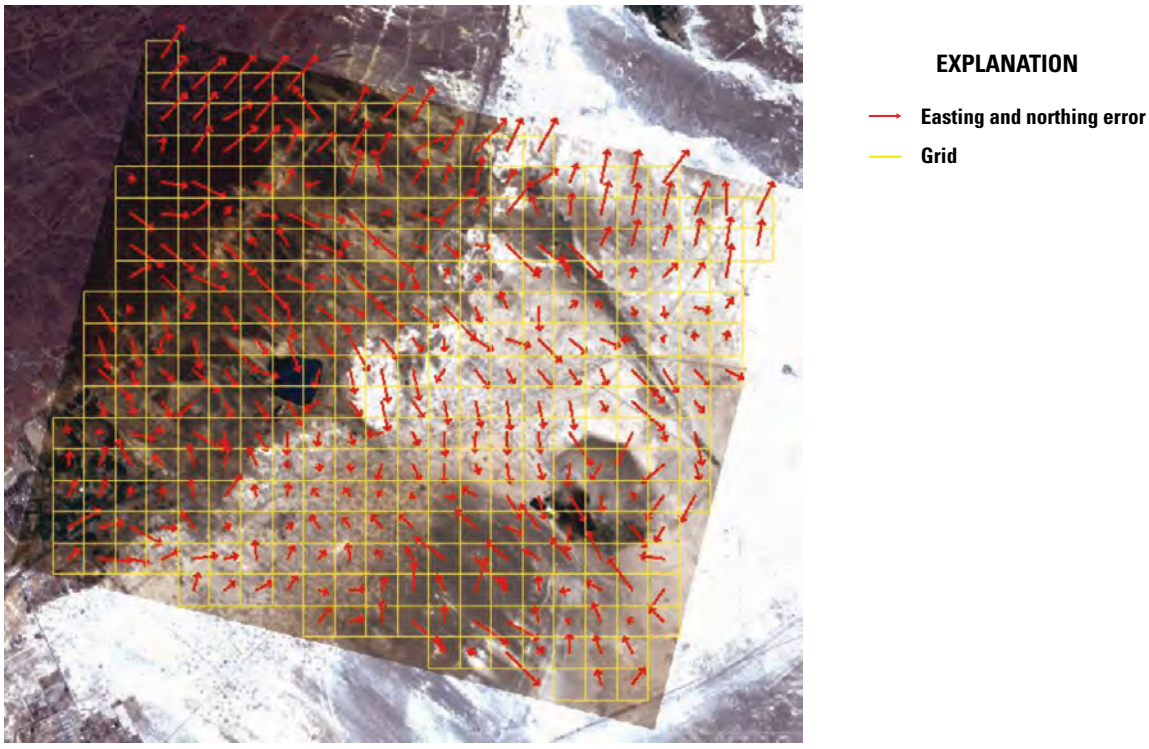

Figure 24. Image-to-image geometric error map with error vector for each grid derived from the Chinese scene pair comprising a Planet Labs PBC Tanager scene (20250523_055213_30_4001) and a Landsat Operational Land Imager scene (LC08_L1TP_145028_20250523_20250602_02_T1). Tanager image copyrighted by Planet Labs PBC, licensed under the Creative Commons Attribution-NonCommercial-ShareAlike 2.0 Generic license. Landsat image by U.S. Geological Survey.

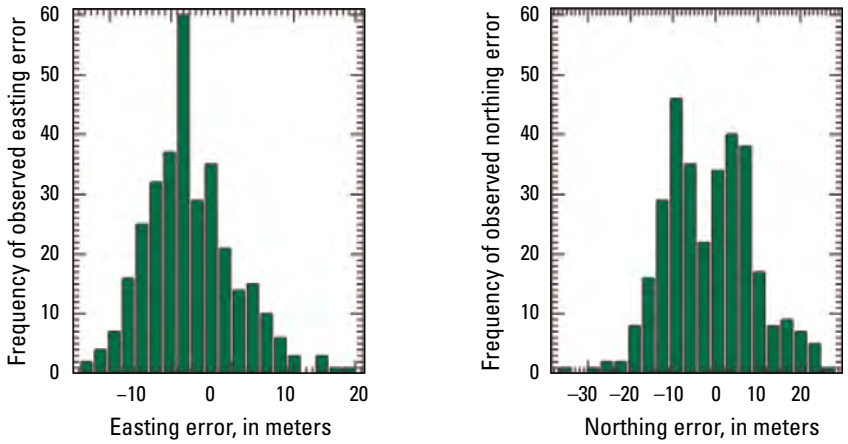

Figure 25. Histogram of image-to-image geometric error derived from the Chinese scene pair comprising a Planet Labs PBC Tanager scene (20250523_055213_30_4001) and a Landsat Operational Land Imager scene (LC08_L1TP_145028_20250523_20250602_02_T1).

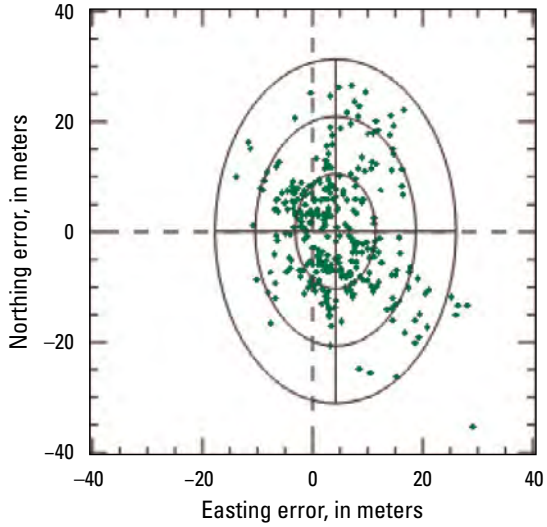

Figure 26. Error scatterplot of image-to-image geometric error derived from the Chinese scene pair comprising a Planet Labs PBC Tanager scene (20250523_055213_30_4001) and a Landsat Operational Land Imager scene (LC08_L1TP_145028_20250523_20250602_02_T1).

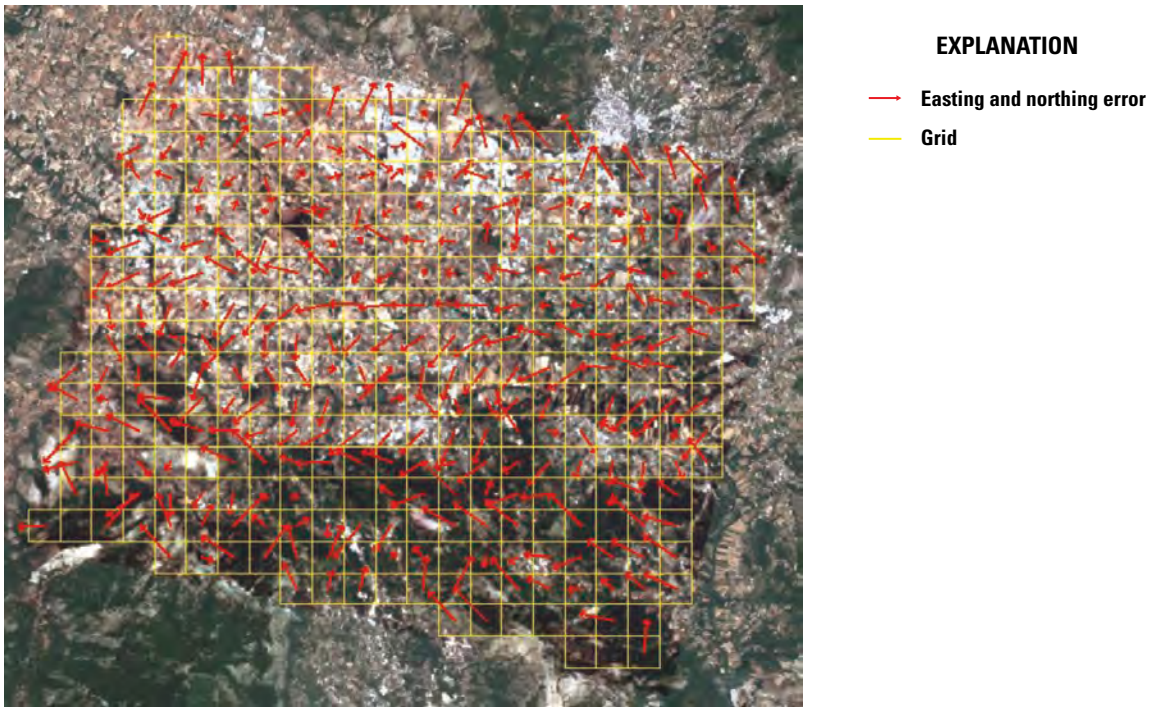

Figure 27. Image-to-image geometric error map with error vector for each grid derived from the Italian scene pair comprising a Planet Labs PBC Tanager scene (20250627_103759_58_4001) and a Landsat Operational Land Imager scene (LC09_L1TP_190031_20250627_20250627_02_T1). Tanager image copyrighted by Planet Labs PBC, licensed under the Creative Commons Attribution-NonCommercial-ShareAlike 2.0 Generic license. Landsat image by U.S. Geological Survey.

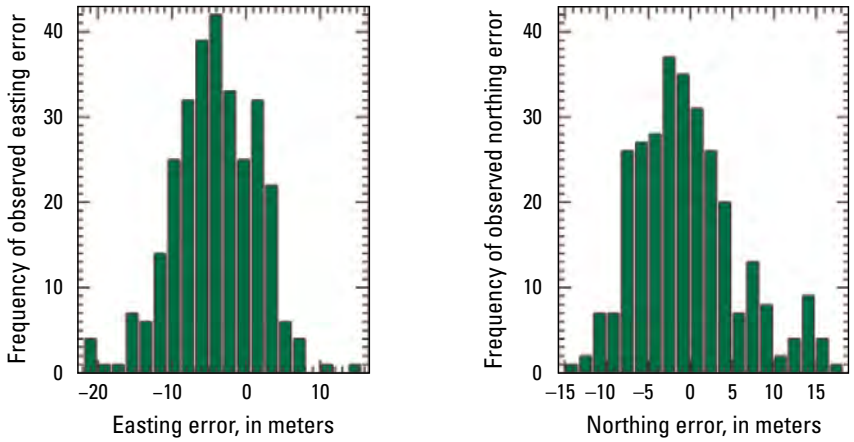

Figure 28. Histogram of image-to-image geometric error derived from the Italian scene pair comprising a Planet Labs PBC Tanager scene (20250627_103759_58_4001) and a Landsat Operational Land Imager scene (LC09_L1TP_190031_20250627_20250627_02_T1).

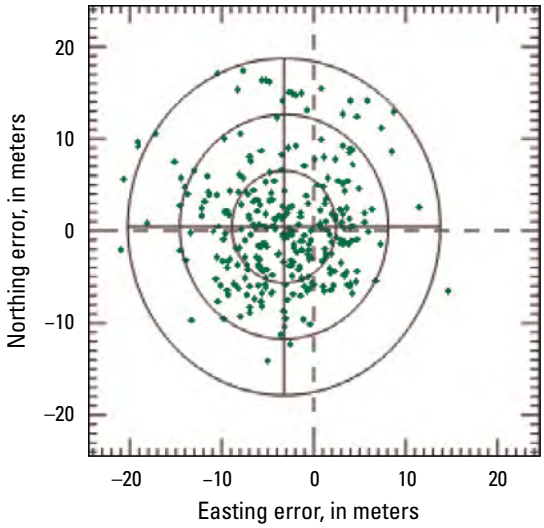

Figure 29. Error scatterplot of image-to-image geometric error derived from the Italian scene pair comprising a Planet Labs PBC Tanager scene (20250627_103759_58_4001) and a Landsat Operational Land Imager scene (LC09_L1TP_190031_20250627_20250627_02_T1).

Table 6. Top of Atmosphere reflectance comparison of the Planet Labs PBC Tanager and Landsat Operational Land Imager.

[OLI, Operational Land Imager; ID, identifier; B, band; CA, coastal aerosol; NIR, near infrared; SW1, shortwave infrared 1; SW2, shortwave infrared 2; %, percent; R^2, coefficient of determination]

Scene location	Scene pair		Statistics	B1 (CA)	B2 (blue)	B3 (green)	B4 (red)	B5 (NIR)	B6 (SW1)	B7 (SW2)
	Tanager scene ID	Landsat OLI scene ID								
Mojave Desert, Arizona	20250405_190836_16_4001	LC08_L1TP_040035_20250405_20250412_02_T1	Uncertainty (%)	2.554	2.808	4.311	4.285	4.887	4.895	6.803
			R^2	0.947	0.948	0.948	0.947	0.954	0.956	0.955
			Regression offset	0.001	0.001	0.006	0.009	0.006	0.005	0.001
			Regression slope	0.982	0.995	0.994	0.939	0.944	0.953	0.938
India	20250420_060625_00_4001	LC09_L1TP_146043_20250420_20250420_02_T1	Uncertainty (%)	4.765	6.56	8.338	4.277	3.816	3.515	4.34
			R^2	0.899	0.921	0.943	0.948	0.947	0.96	0.966
			Regression offset	0.008	0.007	0.01	0.017	0.026	0.027	0.014
			Regression slope	0.997	1.014	1.01	0.923	0.904	0.909	0.919
Sudan	20250502_090330_87_4001	LC08_L1TP_174049_20250502_20250508_02_T1	Uncertainty (%)	2.900	3.700	5.100	5.590	5.570	5.400	5.520
			R^2	0.936	0.931	0.922	0.915	0.926	0.934	0.936
			Regression offset	−0.004	0.001	0.005	0.011	0.005	0.020	0.016
			Regression slope	1.006	1.010	1.025	0.989	1.007	0.975	0.960
Australia	20250305_010639_32_4001	LC09_L1TP_096076_20250305_20250305_02_T1	Uncertainty (%)	4.920	7.113	11.224	8.836	6.466	8.142	6.376
			R^2	0.870	0.888	0.900	0.886	0.928	0.897	0.904
			Regression offset	0.013	0.010	0.014	0.023	0.023	0.045	0.027
			Regression slope	0.950	0.978	0.980	0.896	0.940	0.902	0.905
China	20250523_055213_30_4001	LC08_L1TP_145028_20250523_20250602_02_T1	Uncertainty (%)	6.361	8.214	8.753	5.524	5.558	5.279	6.382
			R^2	0.982	0.981	0.979	0.977	0.976	0.973	0.973
			Regression offset	0.000	0.000	0.003	0.006	0.004	0.007	0.002
			Regression slope	1.051	1.066	1.052	0.983	0.976	0.957	0.951
Italy	20250627_103759_58_4001	LC09_L1TP_190031_20250627_20250627_02_T1	Uncertainty (%)	3.714	5.465	8.386	12.578	6.825	9.120	14.251
			R^2	0.876	0.880	0.870	0.888	0.829	0.870	0.887
			Regression offset	0.011	0.009	0.014	0.010	0.056	0.040	0.012
			Regression slope	0.922	0.932	0.906	0.879	0.830	0.834	0.874

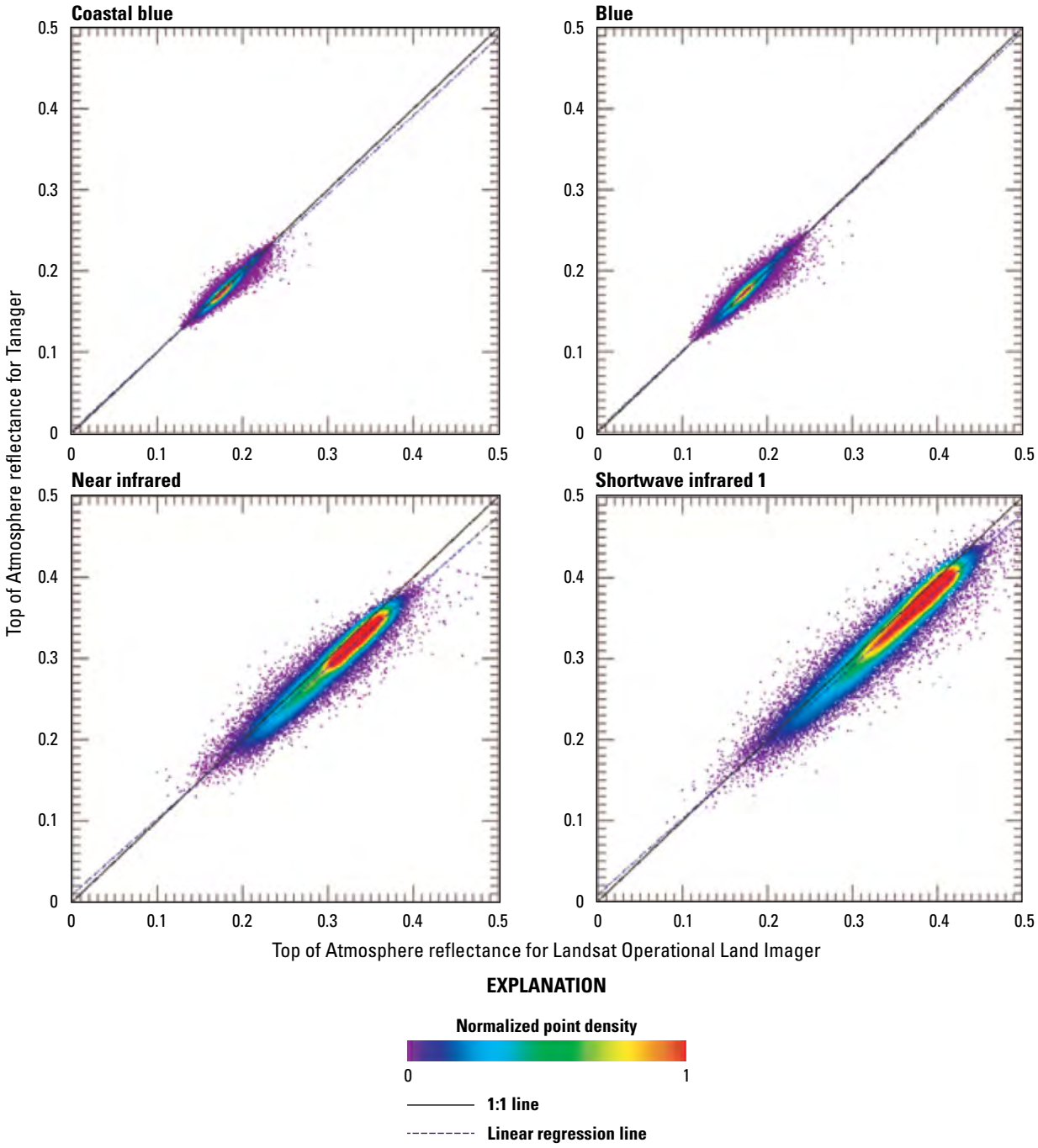

Figure 30. Radiometric scatterplots comparing Top of Atmosphere reflectance values derived from all seven bands of the spectrally resampled Mojave Desert, Arizona, Planet Labs PBC Tanager scene (20250405_190836_16_4001) and Landsat Operational Land Imager scene (LC08_L1TP_040035_20250405_20250412_02_T1).

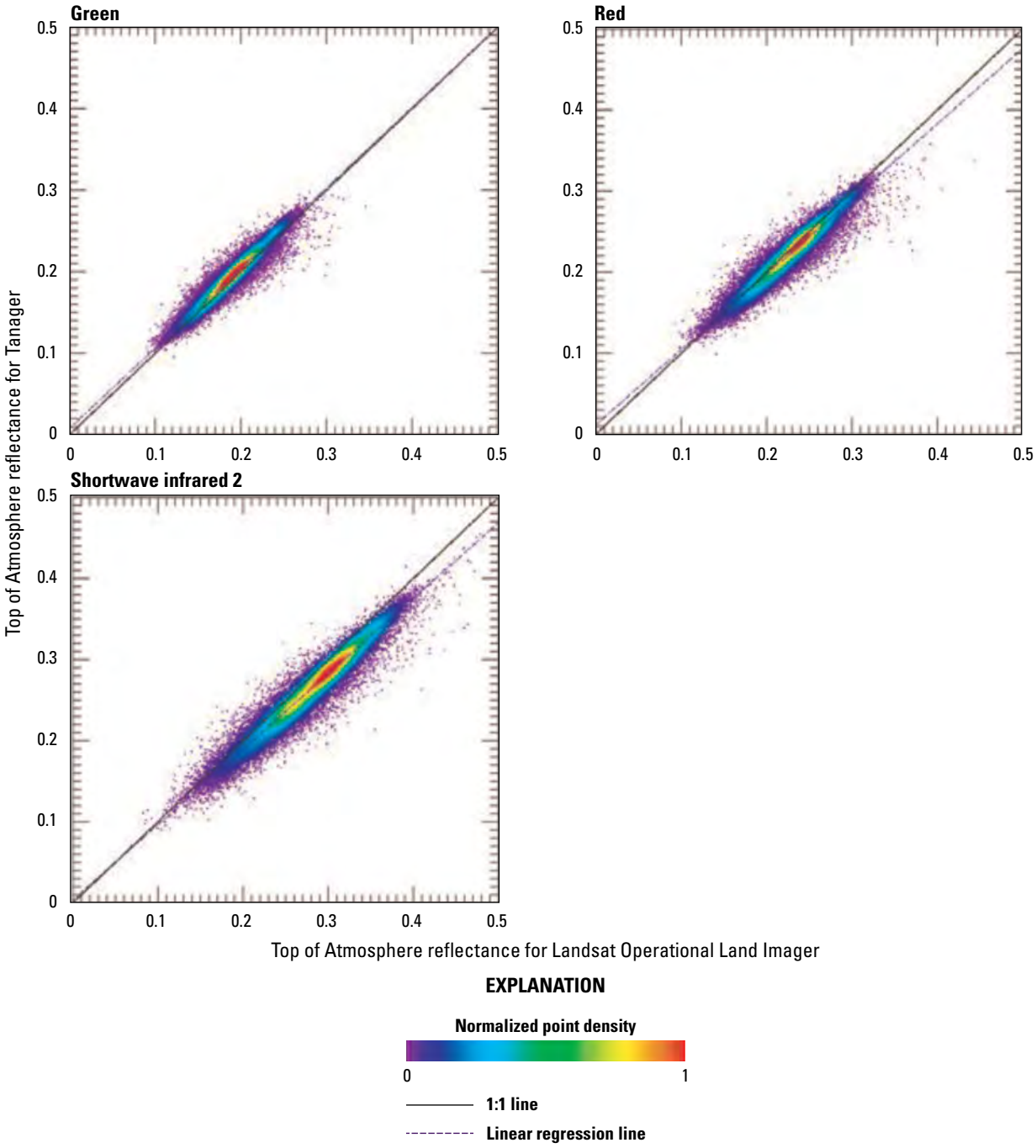

Figure 30. Radiometric scatterplots comparing Top of Atmosphere reflectance values derived from all seven bands of the spectrally resampled Mojave Desert, Arizona, Planet Labs PBC Tanager scene (20250405_190836_16_4001) and Landsat Operational Land Imager scene (LC08_L1TP_040035_20250405_20250412_02_T1).—Continued

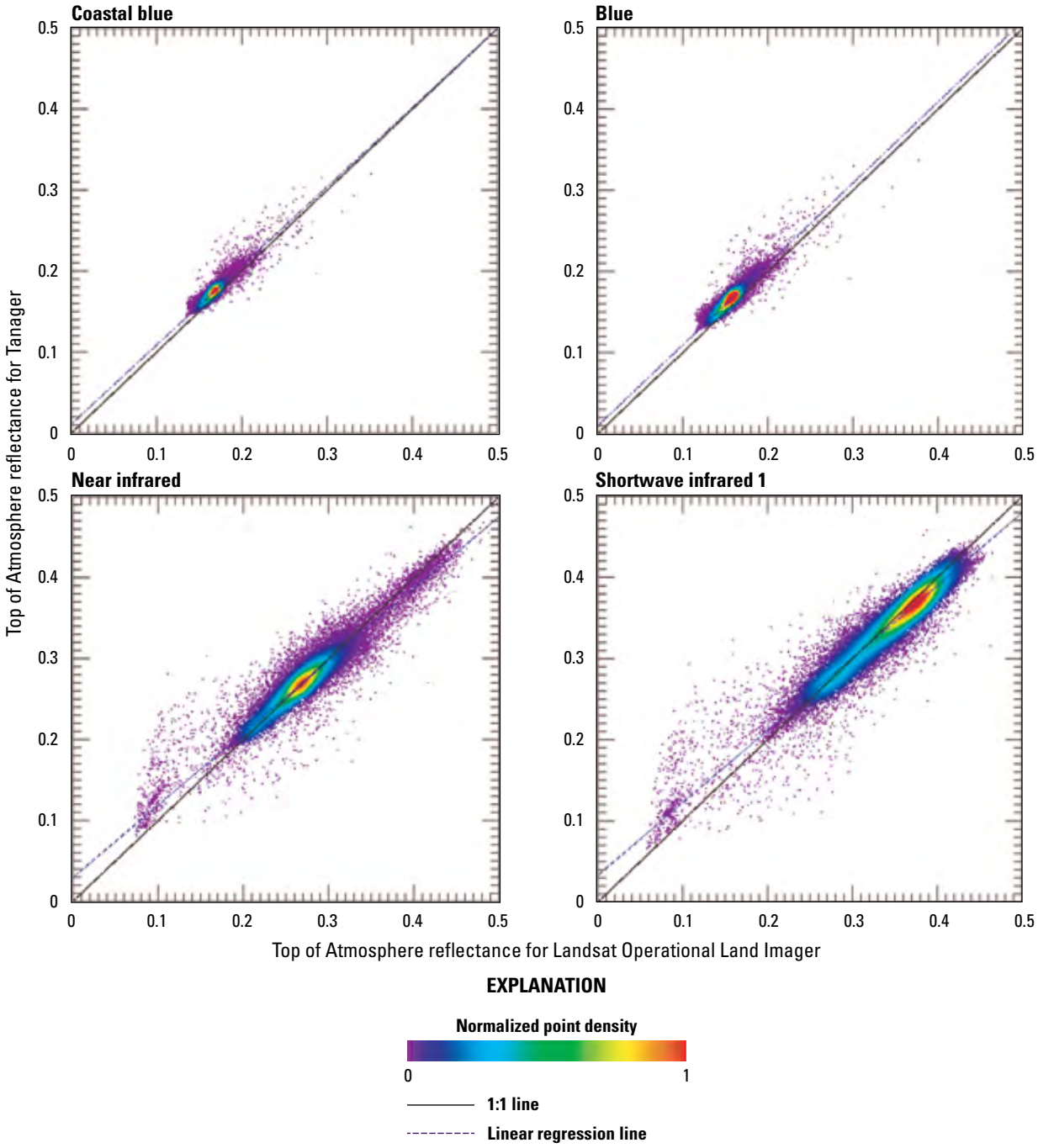

Figure 31. Radiometric scatterplots comparing Top of Atmosphere reflectance values derived from all seven bands of the spectrally resampled Indian Planet Labs PBC Tanager scene (20250420_060625_00_4001) and Landsat Operational Land Imager scene (LC09_L1TP_146043_20250420_20250420_02_T1).

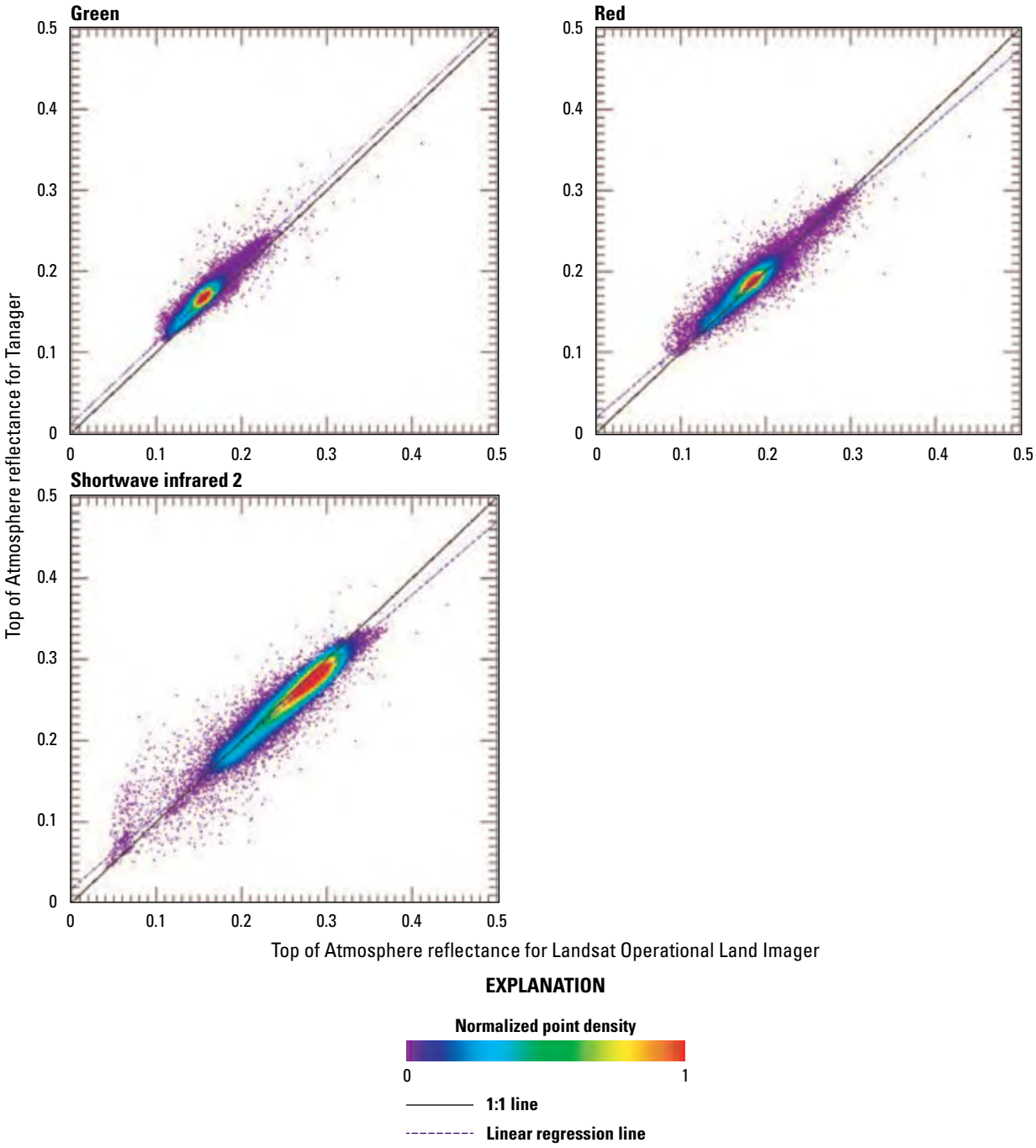

Figure 31. Radiometric scatterplots comparing Top of Atmosphere reflectance values derived from all seven bands of the spectrally resampled Indian Planet Labs PBC Tanager scene (20250420_060625_00_4001) and Landsat Operational Land Imager scene (LC09_L1TP_146043_20250420_20250420_02_T1).—Continued

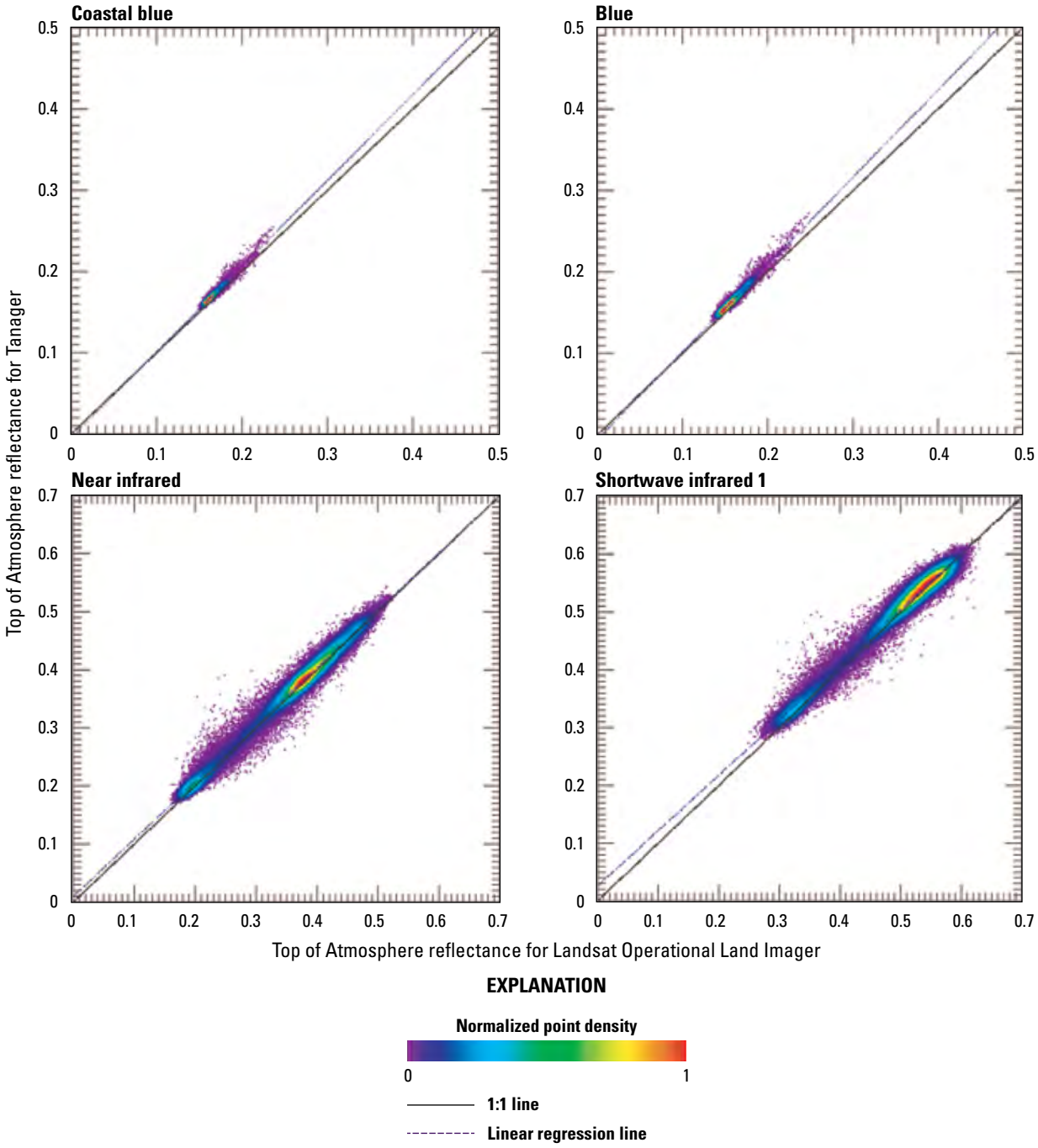

Figure 32. Radiometric scatterplots comparing Top of Atmosphere reflectance values derived from all seven bands of the spectrally resampled Sudanese Planet Labs PBC Tanager scene (20250502_090330_87_4001) and Landsat Operational Land Imager scene (LC08_L1TP_174049_20250502_20250508_02_T1).

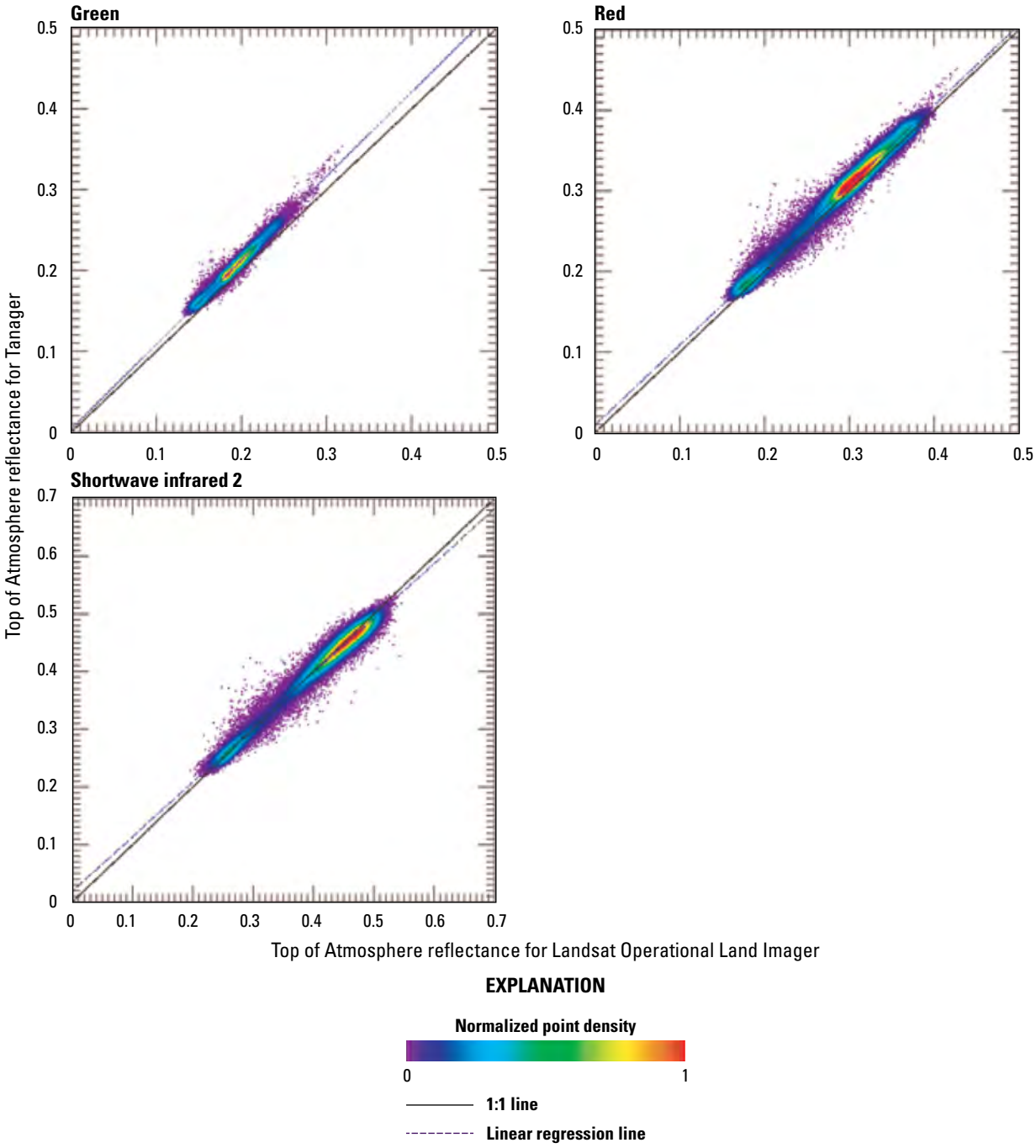

Figure 32. Radiometric scatterplots comparing Top of Atmosphere reflectance values derived from all seven bands of the spectrally resampled Sudanese Planet Labs PBC Tanager scene (20250502_090330_87_4001) and Landsat Operational Land Imager scene (LC08_L1TP_174049_20250502_20250508_02_T1).—Continued

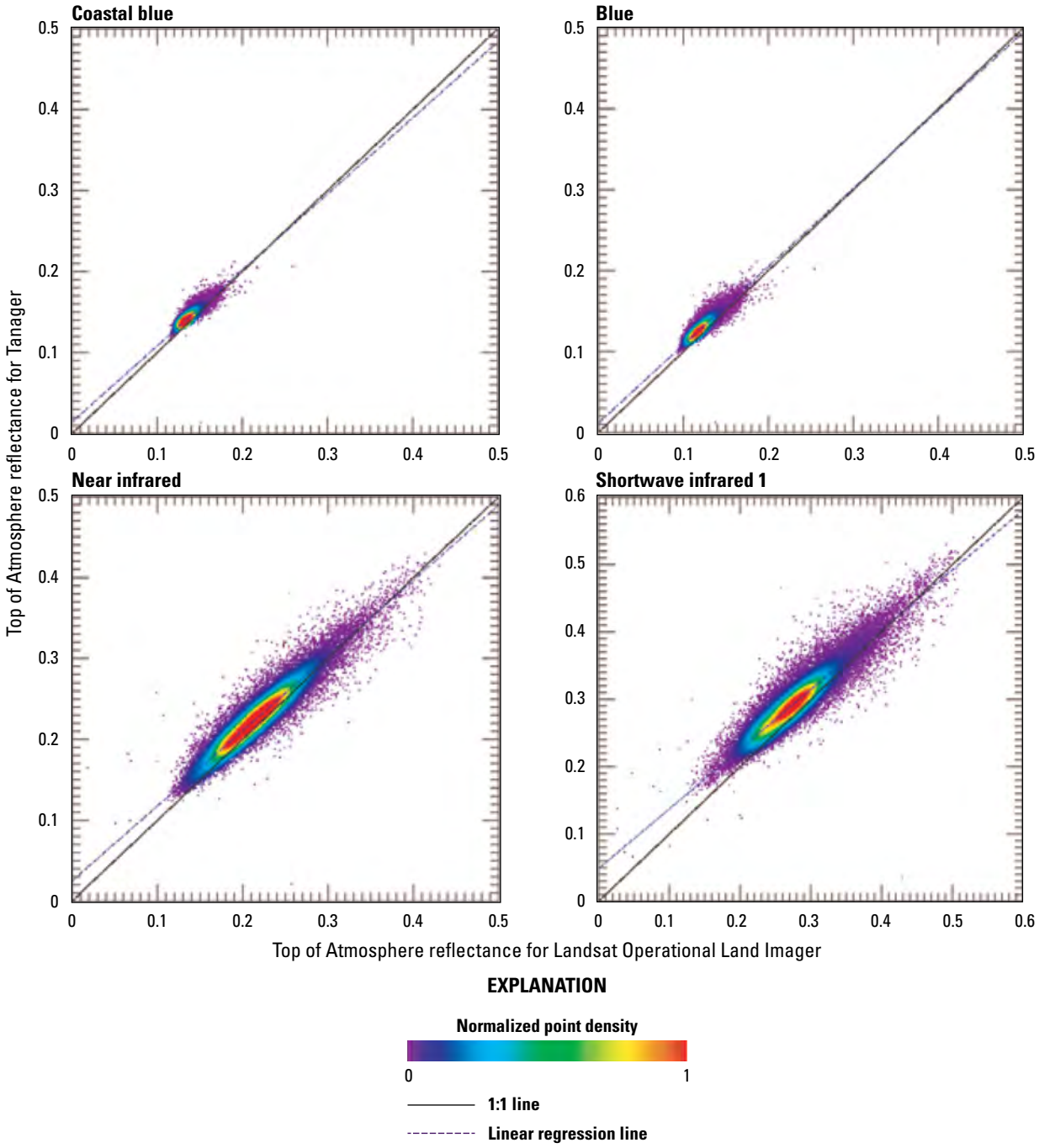

Figure 33. Radiometric scatterplots comparing Top of Atmosphere reflectance values derived from all seven bands of the spectrally resampled Australian Planet Labs PBC Tanager scene (20250305_010639_32_4001) and Landsat Operational Land Imager scene (LC09_L1TP_096076_20250305_20250305_02_T1).

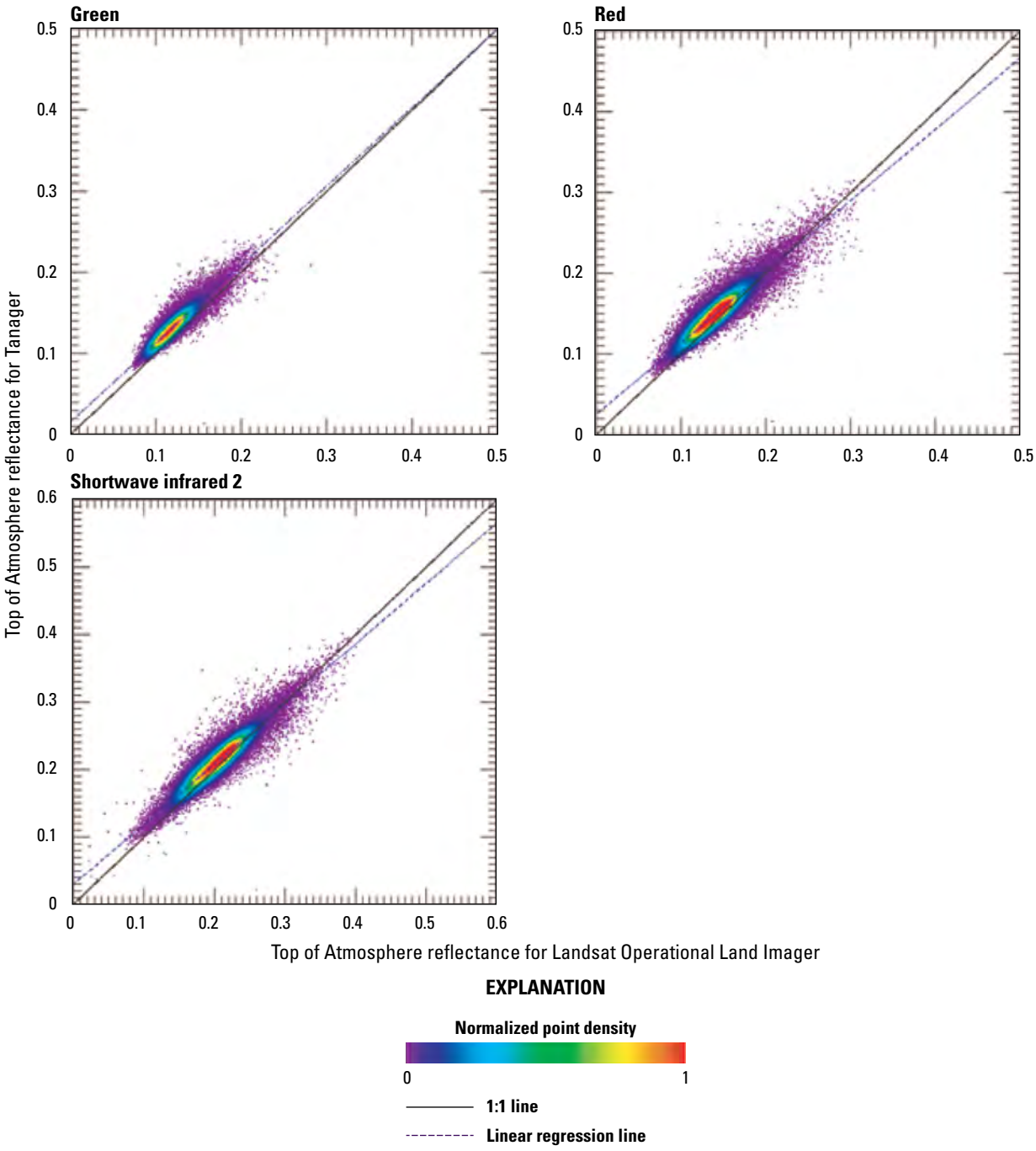

Figure 33. Radiometric scatterplots comparing Top of Atmosphere reflectance values derived from all seven bands of the spectrally resampled Australian Planet Labs PBC Tanager scene (20250305_010639_32_4001) and Landsat Operational Land Imager scene (LC09_L1TP_096076_20250305_20250305_02_T1.—Continued

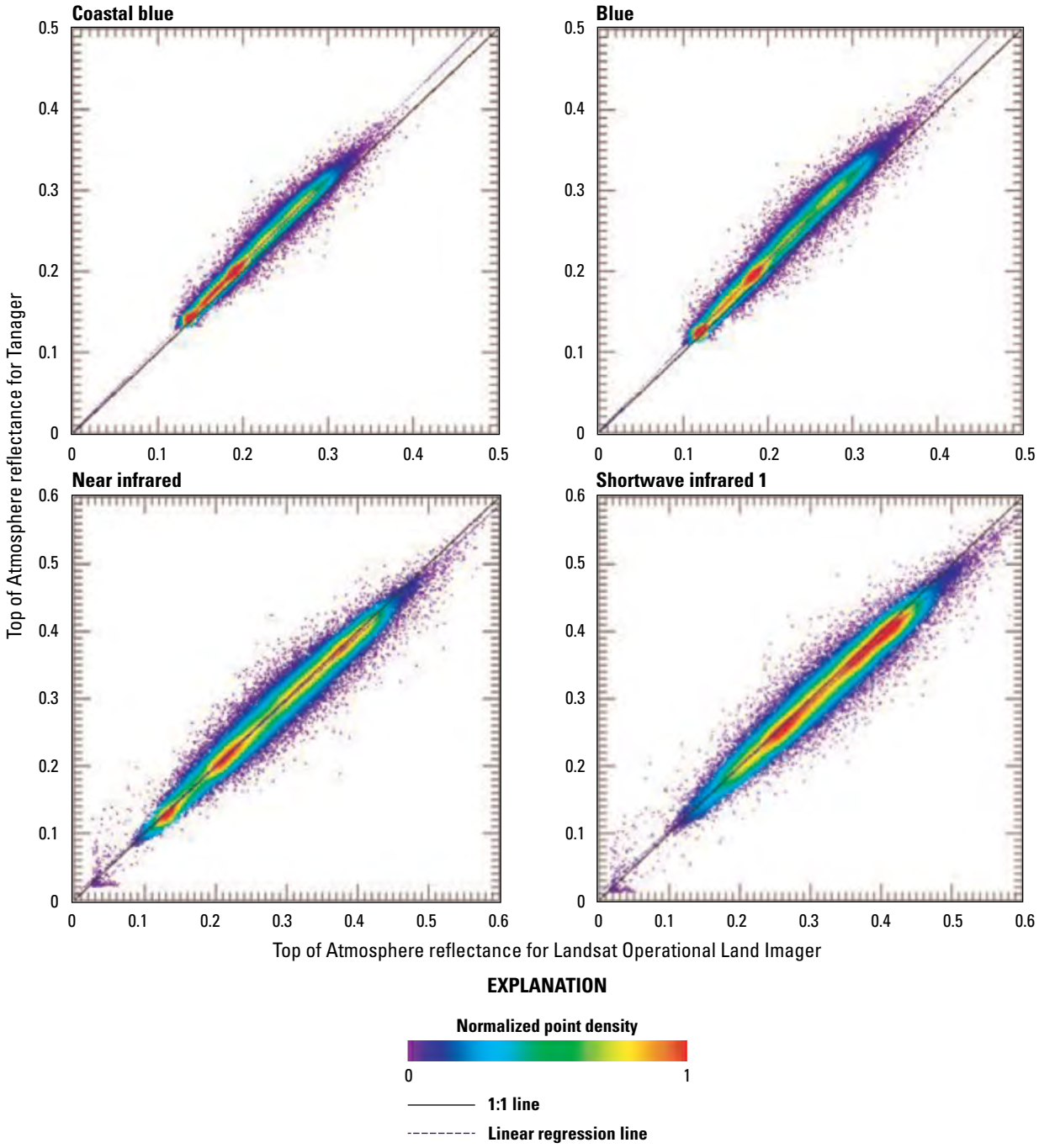

Figure 34. Radiometric scatterplots comparing Top of Atmosphere reflectance values derived from all seven bands of the spectrally resampled Chinese Planet Labs PBC Tanager scene (20250523_055213_30_4001) and Landsat Operational Land Imager scene (LC08_L1TP_145028_20250523_20250602_02_T1).

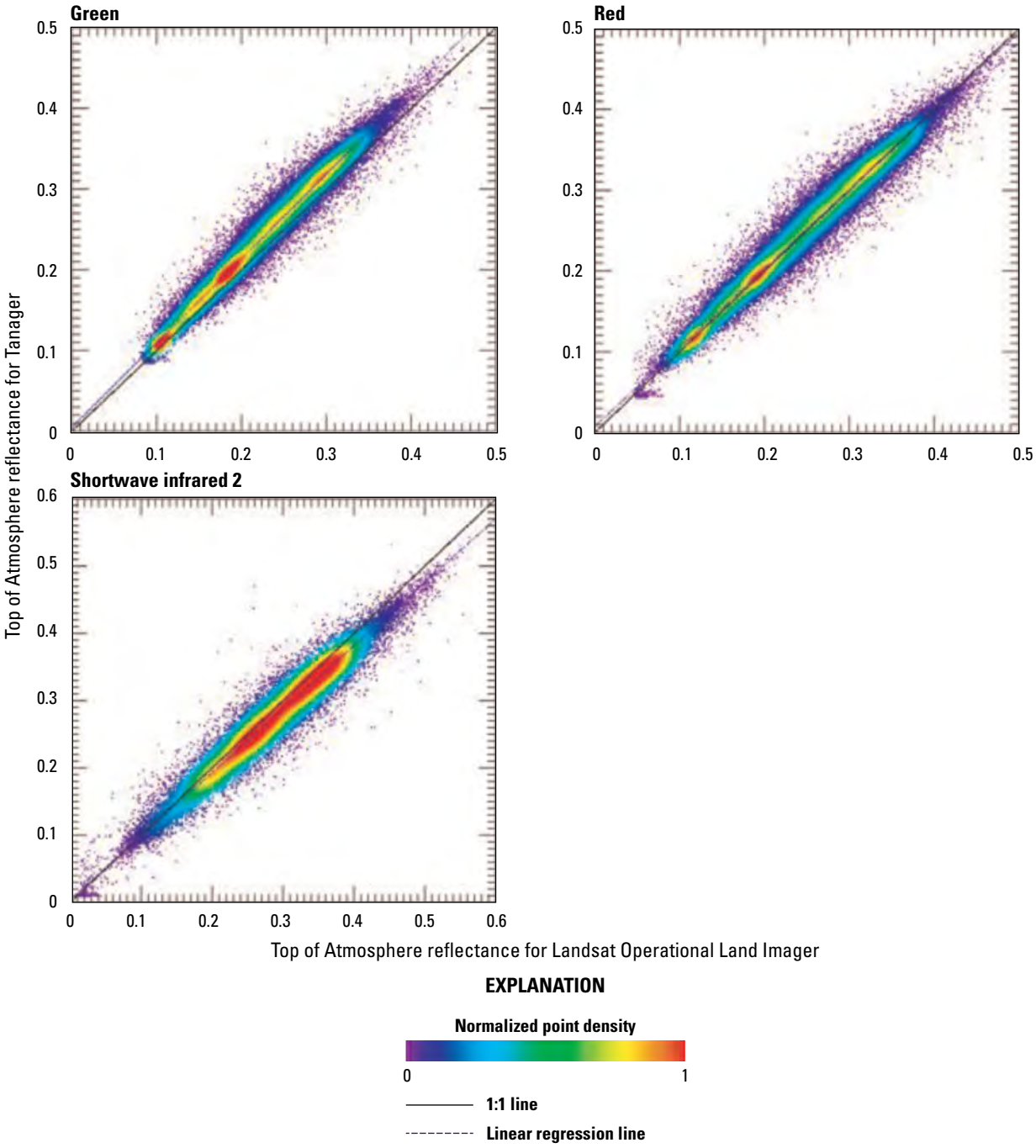

Figure 34. Radiometric scatterplots comparing Top of Atmosphere reflectance values derived from all seven bands of the spectrally resampled Chinese Planet Labs PBC Tanager scene (20250523_055213_30_4001) and Landsat Operational Land Imager scene (LC08_L1TP_145028_20250523_20250602_02_T1).—Continued

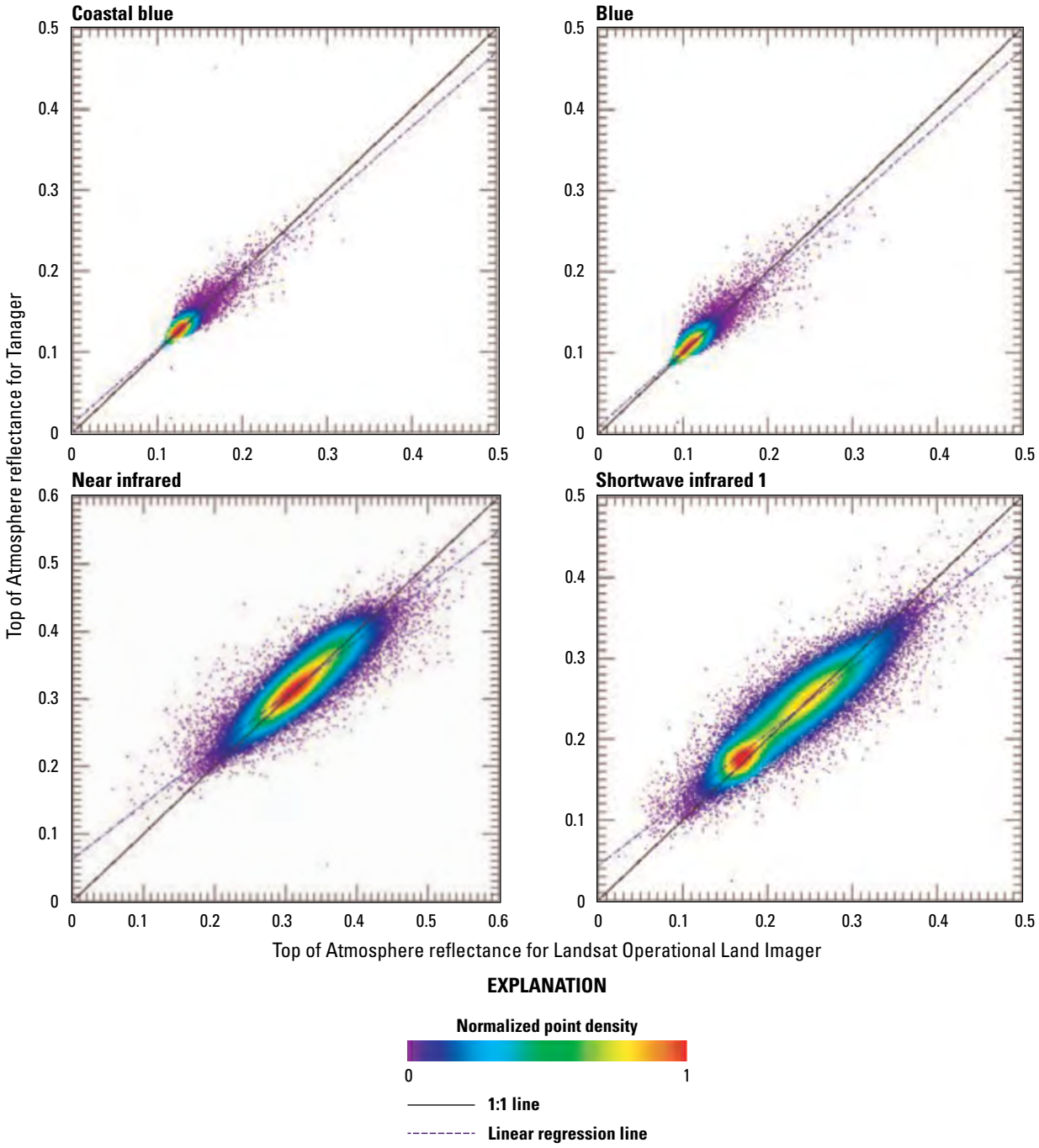

Figure 35. Radiometric scatterplots comparing Top of Atmosphere reflectance values derived from all seven bands of the spectrally resampled Italian Planet Labs PBC Tanager scene (20250627_103759_58_4001) and Landsat Operational Land Imager scene (LC09_L1TP_190031_20250627_20250627_02_T1).

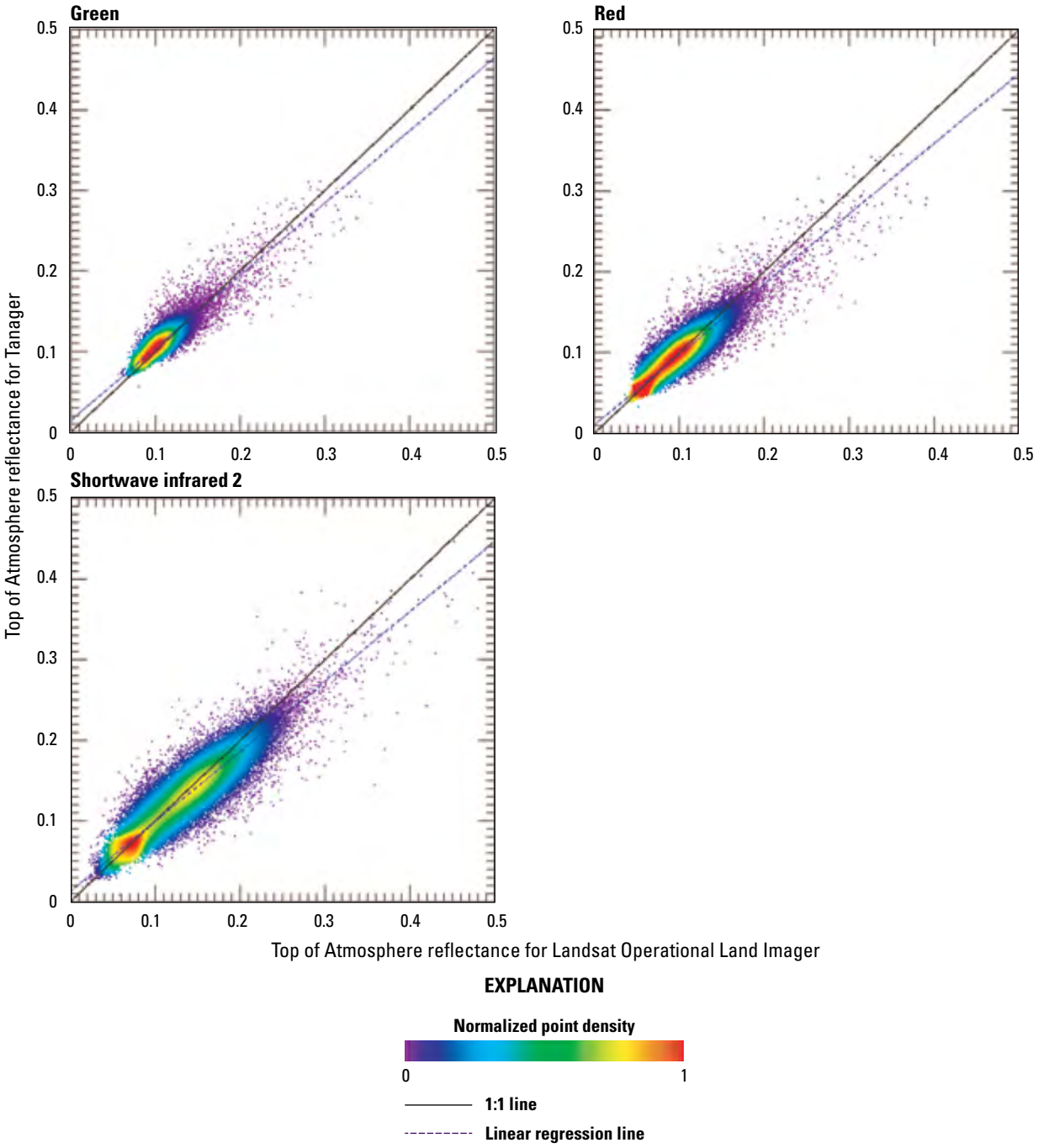

Figure 35. Radiometric scatterplots comparing Top of Atmosphere reflectance values derived from all seven bands of the spectrally resampled Italian Planet Labs PBC Tanager scene (20250627_103759_58_4001) and Landsat Operational Land Imager scene (LC09_L1TP_190031_20250627_20250627_02_T1).—Continued

Comparison to Radiometric Calibration Network

The Tanager hyperspectral data were cross-checked against Radiometric Calibration Network (RadCalNet) data (https://www.radcalnet.org; RadCalNet, 2026).

The region of interest for the hyperspectral TOAR comparison was Railroad Valley, Nevada. The Tanager scenes used were collected on April 19, 2025 (20250419_190925_16_4001), and May 10, 2025 (20250510_191209_16_4001). The scenes were compared to the RadCalNet dataset RVUS_2025_109 and dataset RVUS_2025_130, respectively. The comparison plots for Tanager scenes and RadCalNet data are shown in figures 36 and 37.

Spectral Shift

The sharp spectral absorption feature around the oxygen A-band near the 760-nm region provides a chance to evaluate spectral shift. The precisely known high resolution absorption of the sharp oxygen A-band region can be resampled using the spectral response function of Tanager. A look-up table around the oxygen A-band at several nominal Tanager hyperspectral bands is created by giving a range of spectral shifts. For a given Tanager scene and for all pixels along the sensor scanline, comparing the Tanager hyperspectral feature to the look-up table enables estimation of spectral shifts for all pixels. The May 10, 2025, Tanager scene over Railroad Valley is used for spectral shift analysis, and the results along the upper and lower scanlines are shown in figures 38 and 39, respectively.

Spatial Performance

Because of the large GSD of the Tanager image, we used a spatial performance analysis technique that uses causeways. The Tanager image used for spatial analysis is 20250524_174343_30_4001. The linear feature in the image is the Lyndon B. Johnson Causeway in Aransas County, Texas (fig. 40).

The geometric parameter for the bridge to generate an analog bridge model is 24.0 m wide, and the orientation angle of the bridge is about 58.66 degrees counterclockwise from east. The analog model is digitized based on the GSD of the image using the variable FWHMs. A simulated bridge image is compared to the sampled bridge image. Because the simulated bridge image is created much larger than the Tanager bridge image segment, the best matching segment out of the simulated image needs to be identified. A cross-correlation matrix is computed, and then the pixel shift that gives the maximum value of the cross-correlation matrix is identified. Once the pixel shift is identified and the matching simulated image segment is clipped, the root mean square difference (RMSD) values between the clipped portion of the simulated bridge with varying FWHMs and the bridge pixels sampled from the Tanager image are compared to find the FWHM associated with the minimum RMSD. The RMSD curve by varying FWHMs ranging from 0.7 to 1.9 pixels is shown in figure 41, and at the minimum position of the curve, an optimized FWHM value for the curve is determined. There are seven curves corresponding to each of the seven bands, and the result is shown in figure 41. All FWHMs determined from the minimum of the RMSD curves can be plotted as a function of wavelength, as shown in figure 42, and it shows the wavelength-dependent trend.

Another Tanager image used for spatial analysis is 20250520_171558_31_4001. The linear feature in the image is the St. Louis Bay Bridge, Mississippi (fig. 43).

The parameters to generate an analog bridge model are 30.0 m width and 7.07 degrees counterclockwise from east as an orientation angle of the bridge. In figure 44, the RMSD curve is shown by varying FWHMs ranging from 0.7 to 1.9 pixels, and at the minimum position of the curve, an optimized FWHM value for the curve is determined. Seven curves correspond to each of the seven bands, and the result is shown in figure 44. All FWHMs determined from the minimum of the RMSD curves can be plotted as a function of wavelength, as shown in figure 45, which shows the wavelength-dependent trend. Spatial performance analysis results are shown in table 7. Figure 46 illustrates how RER and MTF at Nyquist are estimated from FWHM; one specific FWHM result (1.28) from Lyndon B. Johnson Causeway was used as an example.

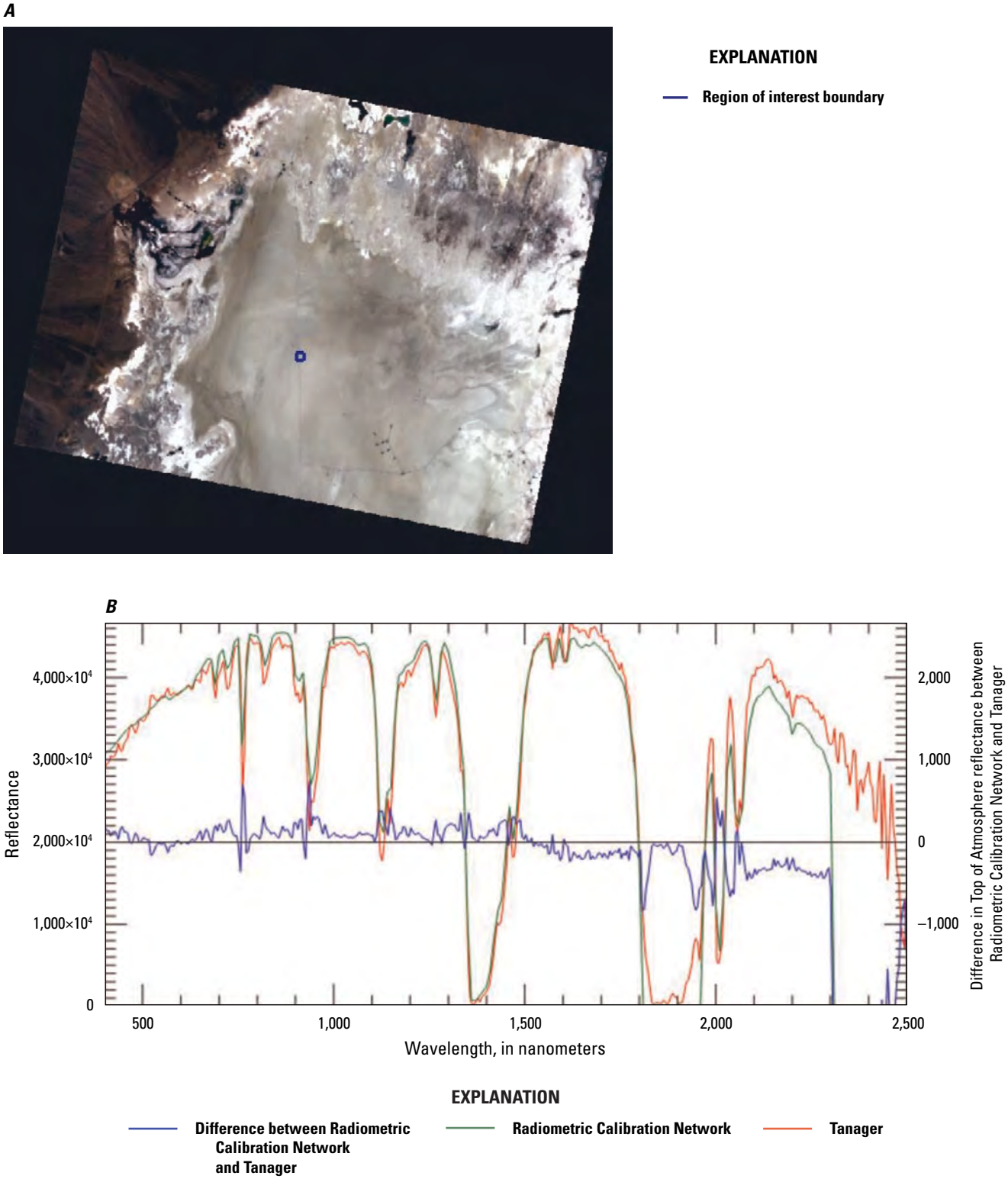

Figure 36. (*A*) Image of Railroad Valley, Nevada, Planet Labs PBC Tanager scene from April 19, 2025 (20250419_190925_16_4001), and (*B*) a graph comparing the Top of Atmosphere reflectance of the Tanager scene and the Radiometric Calibration Network dataset RVUS_2025_109. Image copyrighted by Planet Labs PBC, licensed under the Creative Commons Attribution-NonCommercial-ShareAlike 2.0 Generic license.

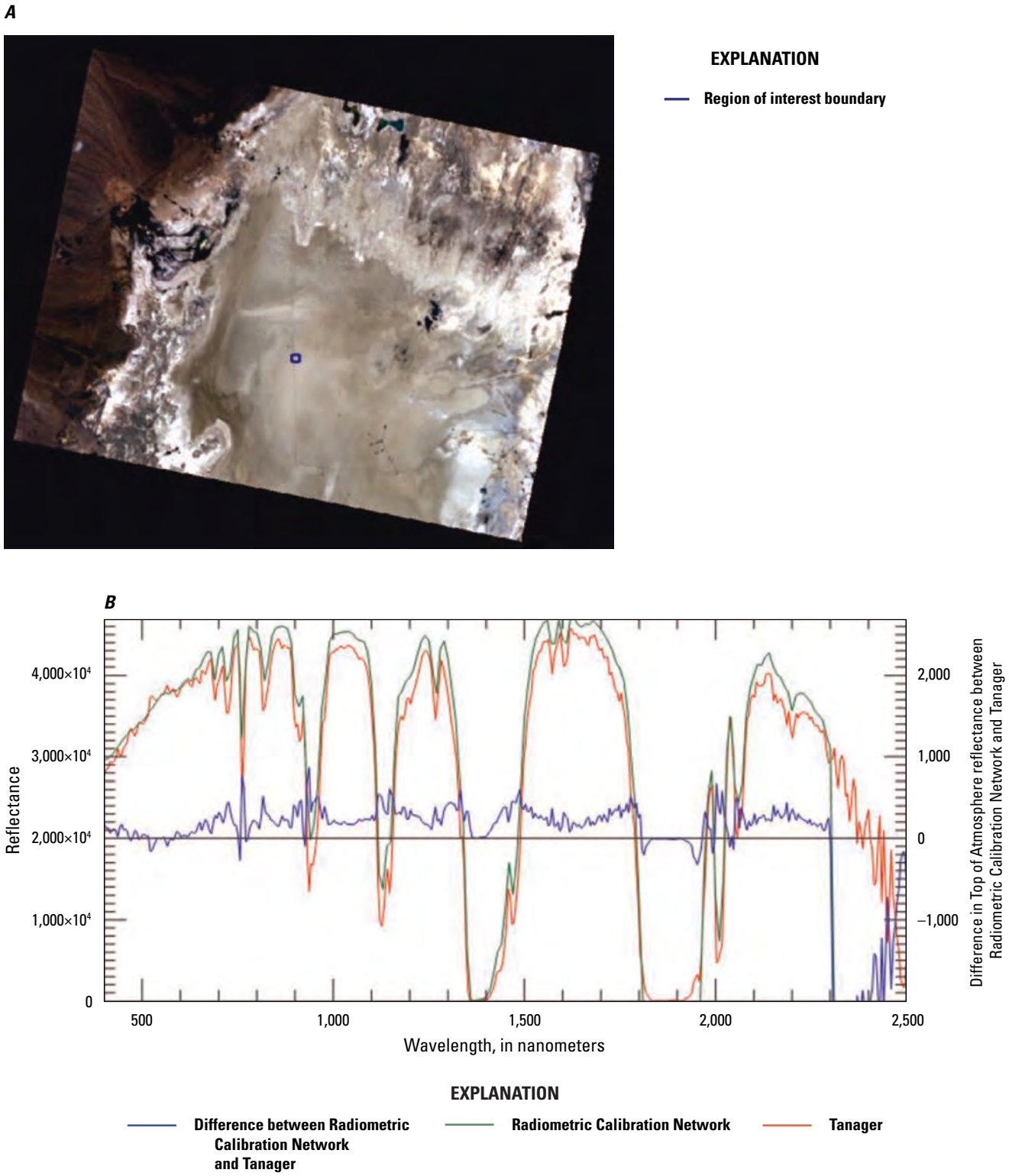

Figure 37. (*A*) Image of Railroad Valley, Nevada, Planet Labs PBC Tanager scene from May 10, 2025 (20250510_191209_16_4001), and (*B*) a graph showing comparing the Top of Atmosphere reflectance of the Tanager scene and the Radiometric Calibration Network dataset RVUS_2025_130. Image copyrighted by Planet Labs PBC, licensed under the Creative Commons Attribution-NonCommercial-ShareAlike 2.0 Generic license.

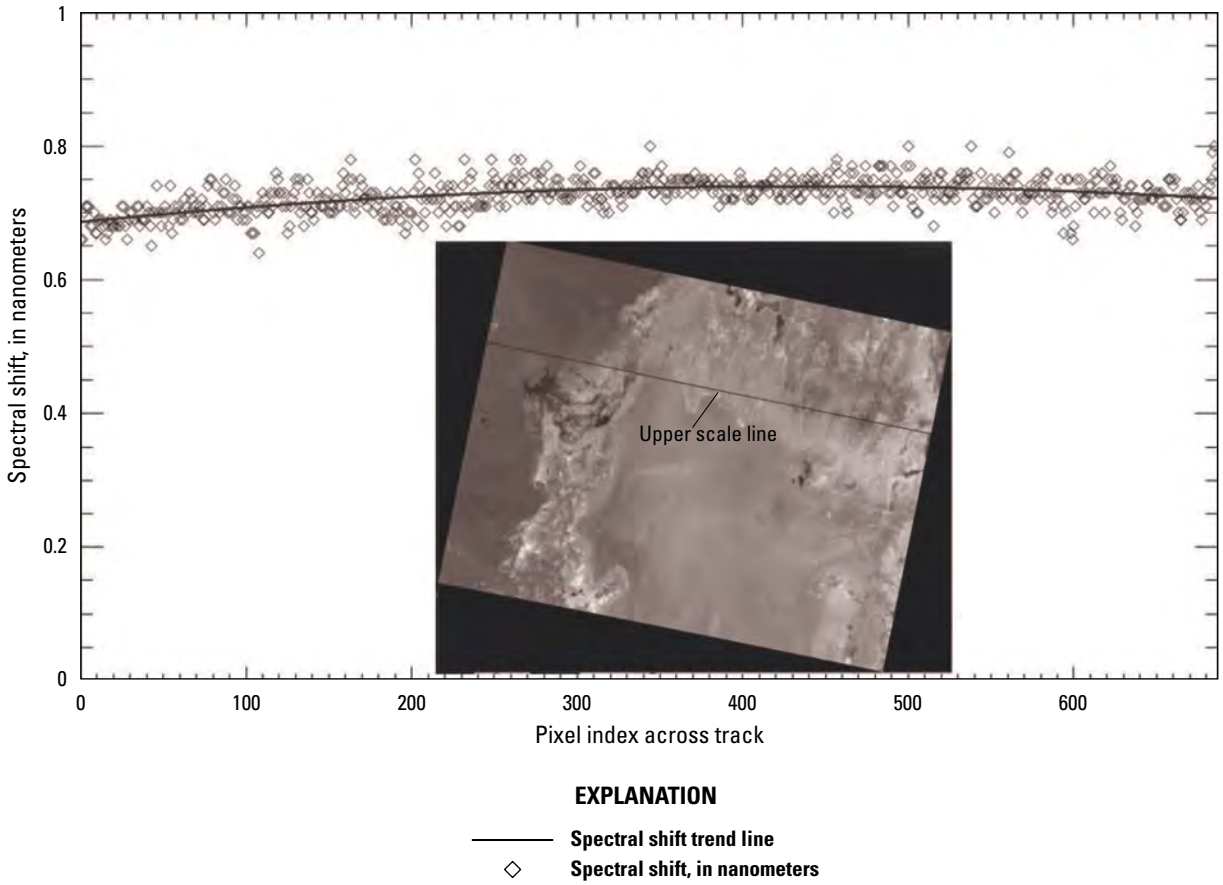

Figure 38. Plot showing the spectral shift analysis results derived from a Railroad Valley, Nevada, Planet Labs PBC Tanager scene (20250510_191209_16_4001) along the upper scanline. Image copyrighted by Planet Labs PBC, licensed under the Creative Commons Attribution-NonCommercial-ShareAlike 2.0 Generic license.

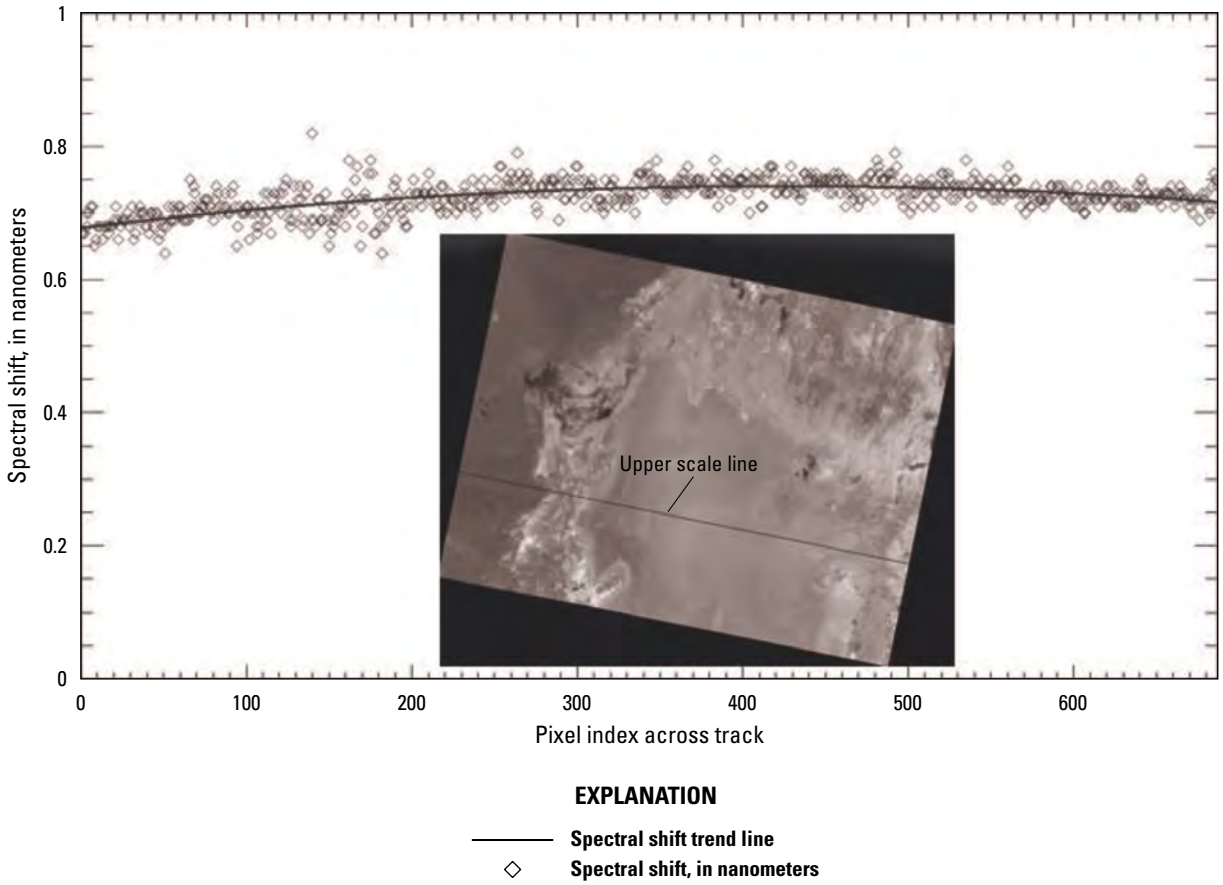

Figure 39. Plot showing the spectral shift analysis results derived from a Railroad Valley, Nevada, Planet Labs PBC Tanager scene (20250510_191209_16_4001) along the lower scanline. Image copyrighted by Planet Labs PBC, licensed under the Creative Commons Attribution-NonCommercial-ShareAlike 2.0 Generic license.

EXPLANATION

Region of interest boundary

Figure 40. Image of Lyndon B. Johnson Causeway, Texas, Planet Labs PBC Tanager scene (20250524_174343_30_4001). The red box emphasizes a region of interest for spatial analysis on the Lyndon B. Johnson Causeway. Image copyrighted by Planet Labs PBC, licensed under the Creative Commons Attribution-NonCommercial-ShareAlike 2.0 Generic license.

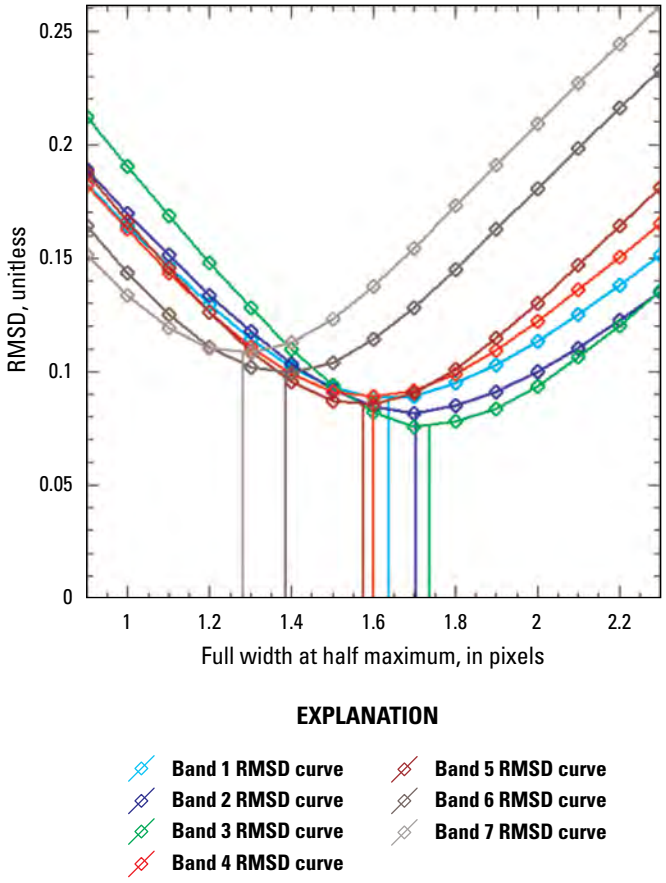

Figure 41. Graph of root mean square difference (RMSD) curves and corresponding minimum full width at half maximum lines for all bands derived from the Lyndon B. Johnson Causeway, Texas, Planet Labs PBC Tanager scene (20250524_174343_30_4001).

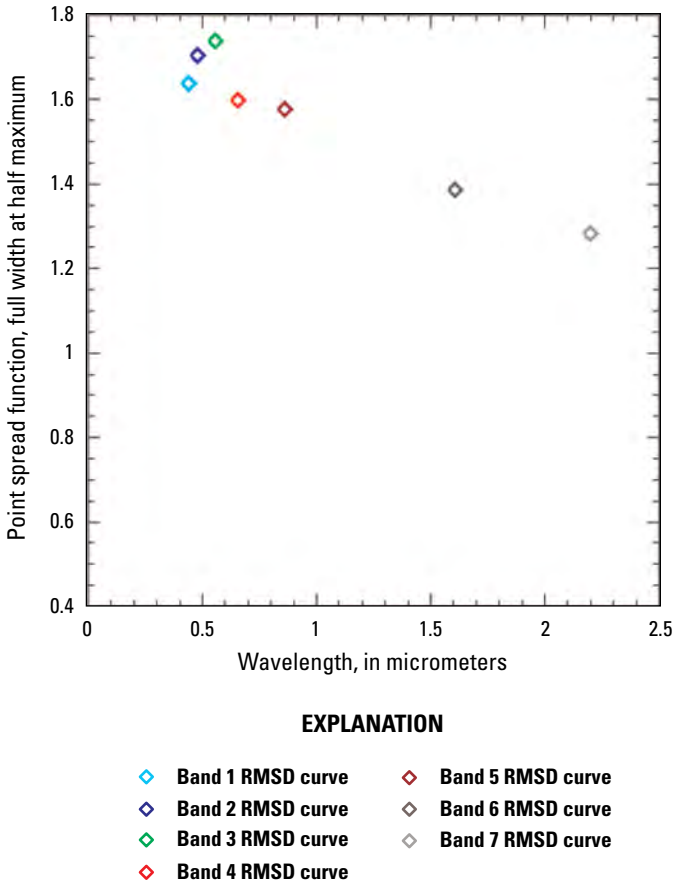

Figure 42. Graph of full width at half maximum for all bands derived from the Lyndon B. Johnson Causeway, Texas, Planet Labs PBC Tanager scene (20250524_174343_30_4001). [RMSD, root mean square difference]

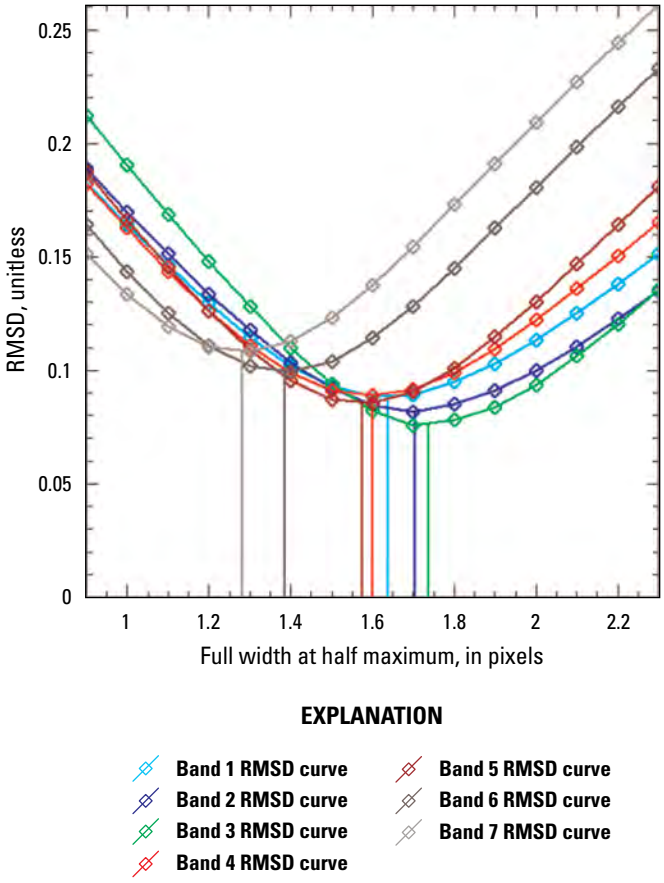

Figure 44. Root mean square difference (RMSD) curves and corresponding minimum full width at half maximum lines for all bands derived from the St. Louis Bay Bridge, Mississippi, Planet Labs PBC Tanager scene (20250520_171558_31_4001).

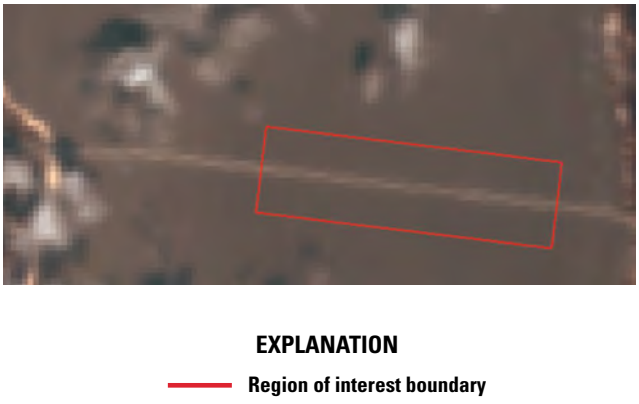

Figure 43. Image of St. Louis Bay Bridge, Mississippi, Planet Labs PBC Tanager scene (20250520_171558_31_4001). The red box emphasizes a region of interest for spatial analysis on the St. Louis Bay Bridge. Image copyrighted by Planet Labs PBC, licensed under the Creative Commons Attribution-NonCommercial-ShareAlike 2.0 Generic license.

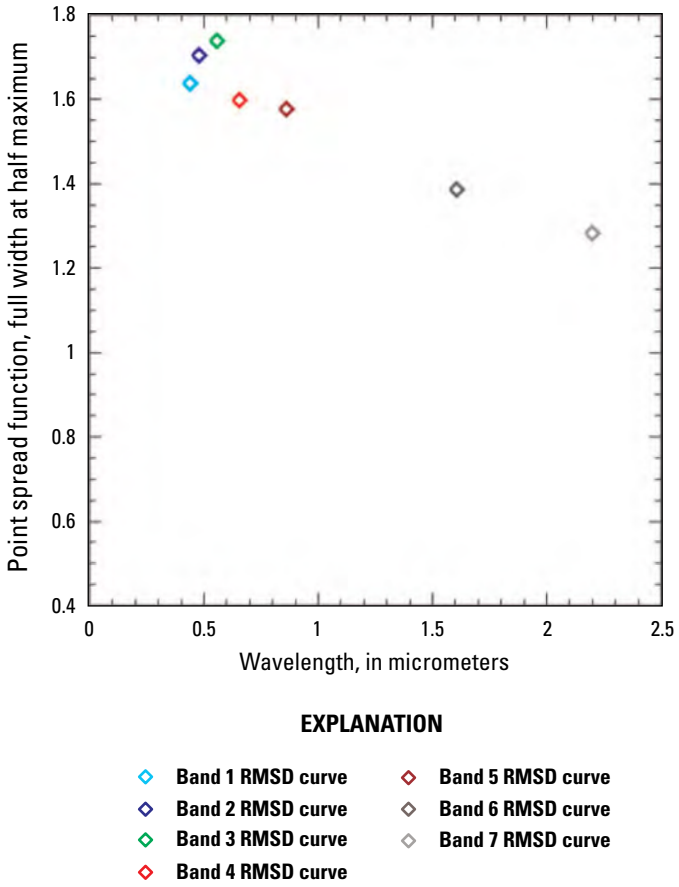

Figure 45. Full width at half maximum for all bands derived from the St. Louis Bay Bridge, Mississippi, Planet Labs PBC Tanager scene (20250520_171558_31_4001). [RMSD, root mean square difference]

Table 7. Spatial performance of the Planet Labs PBC Tanager over the Lyndon B. Johnson Causeway, Texas, and the St. Louis Bay Bridge, Mississippi.

[ID, identifier; RER, relative edge response; FWHM, full width at half maximum; MTF, modulation transfer function]

Scene location	Tanager scene ID	RER	FWHM (pixels)	MTF at Nyquist
Lyndon B. Johnson Causeway, Texas	20250524_174343_30_4001	0.793 to 0.651	1.28 to 1.75	0.482 to 0.253
St. Louis Bay Bridge, Mississippi	20250520_171558_31_4001	0.802 to 0.658	1.27 to 1.74	0.488 to 0.258

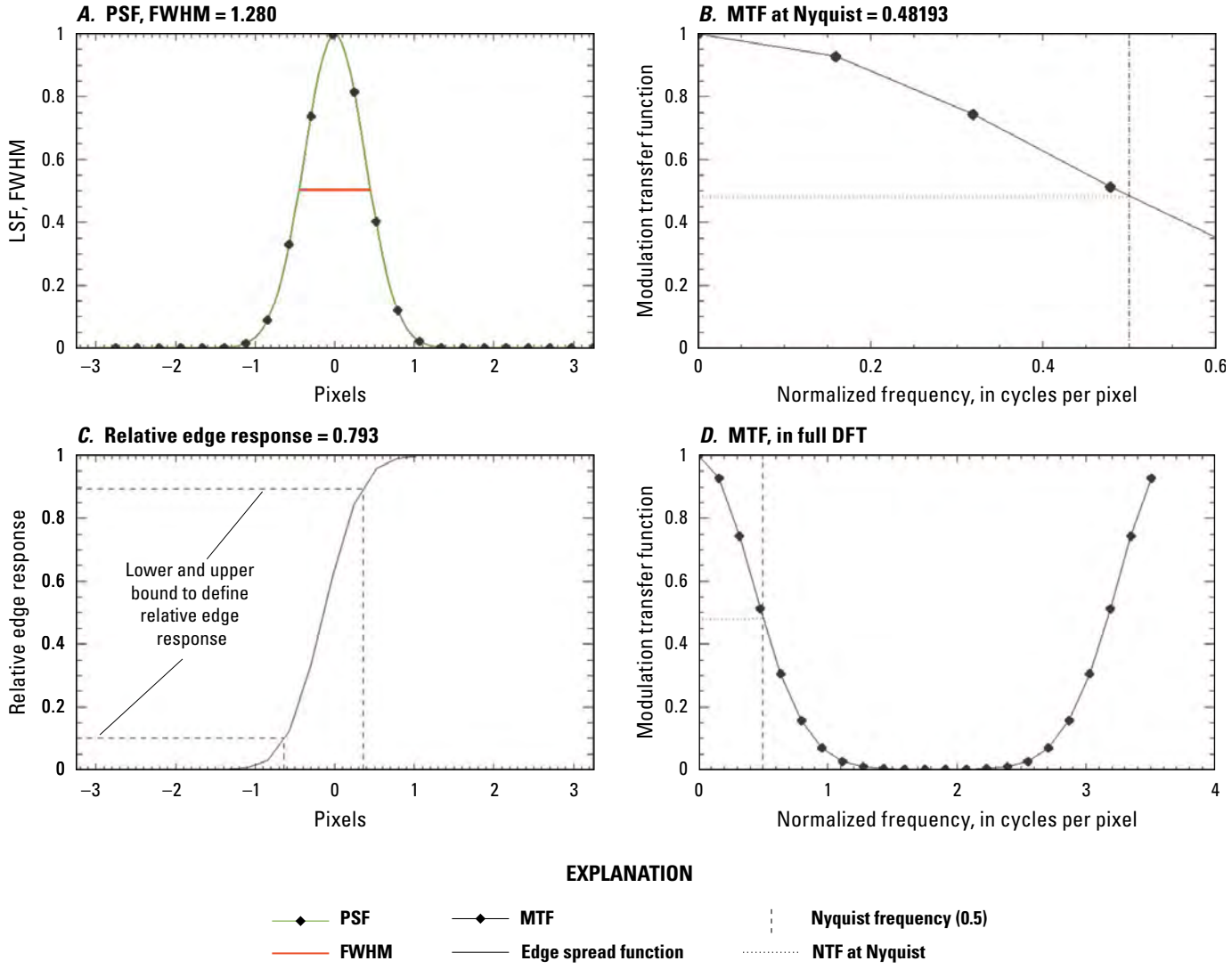

Figure 46. Graphs showing (*A*) point spread function with full width at half maximum in red line (upper left), (*B*) modulation transfer function with Nyquist frequency marked with a vertical dashed line, (*C*) relative edge response with lower and upper bound of the central one pixel marked with dashed lines (lower left), and (*D*) modulation transfer function in full range with Nyquist frequency marked with a vertical dashed line. [PSF, point spread function; FWHM, full width at half maximum; MTF, modulation transfer function; LSF, line spread function; DFT, discrete Fourier transform; one specific FWHM (1.28) from Lyndon B. Johnson Causeway was used to illustrate spatial analysis plots in this figure]

Summary and Conclusions

This report summarizes the sensor performance of the Planet Labs PBC Tanager satellite hyperspectral sensor based on the U.S. Geological Survey Earth Resources Observation and Science Cal/Val Center of Excellence (ECCOE) system characterization process. In summary, we have determined that Tanager has a band-to-band geometric performance in the range of −0.074 to 0.097 pixel, geometric performance relative to the Operational Land Imager in the range of −5.980 meters (−0.20 pixel) to 11.948 meters (0.40 pixel) offset in comparison to Landsat Operational Land Imager, offset of a radiometric comparison in the range of −0.004 to 0.056, slope of a radiometric comparison in the range of 0.830 to 1.066, and spectral shift in the range of 0.65 to 0.75 nanometer. The analysis of the point spread function gives the full width at half maximum in the range of 1.27 to 1.75 pixels, relative edge response in the range of 0.802 to 0.651, and the modulation transfer function at Nyquist in the range of 0.488 to 0.253.

In conclusion, the team has completed an ECCOE standardized system characterization of the Tanager hyperspectral sensor. Although the team followed characterization procedures that are standardized across the many sensors and sensing systems under evaluation, these procedures are customized to fit the individual sensor, as was done with Tanager. The team has acquired data, defined proper testing methodologies, carried out comparative tests against specific references, completed data analyses, and quantified sensor performance accordingly. The team also endeavored to retain all data, measurements, and methods. This is key to ensure that all data and measurements are archived and accessible and that the performance results are reproducible.

The ECCOE project and associated Joint Agency Commercial Imagery Evaluation partners are always interested in reviewing sensor and remote sensing application assessments and would like to review and discuss information on similar data and product assessments and reviews. If you would like to discuss system characterization with the U.S. Geological Survey ECCOE and (or) the Joint Agency Commercial Imagery Evaluation team, please email us at eccoe@usgs.gov.

Selected References

Barsi, J.A., Lee, K., Kvaran, G., Markham, B. L., and Pedelty, J.A., 2014, The spectral response of the Landsat-8 Operational Land Imager: Remote Sensing, v. 6, no. 10, p. 10232–10251, accessed February 13, 2025, at https://doi.org/10.3390/rs61010232.

Cantrell, S.J., and Christopherson, J.B., 2024, Joint Agency Commercial Imagery Evaluation (JACIE) best practices for remote sensing system evaluation and reporting: U.S. Geological Survey Open-File Report 2024–1023, 26 p., accessed August 6, 2024, at https://doi.org/10.3133/ofr20241023.

Planet Labs PBC, 2026, Tanager—Cutting-edge hyperspectral from orbit: Planet Labs PBC website, accessed March 5, 2026, at https://www.planet.com/constellations/tanager/.

RadCalNet, 2026, RadCalNet portal: Working Group on Calibration and Validation of the Committee on Earth Observation Satellites digital data, accessed March 5, 2026, at https://www.radcalnet.org.

U.S. Geological Survey, 2020, EROS CalVal Center of Excellence (ECCOE): U.S. Geological Survey website, accessed March 2021 at https://www.usgs.gov/core-science-systems/eros/calval.

U.S. Geological Survey, 2025, Landsat satellite missions: U.S. Geological Survey website, accessed February 13, 2025, at https://www.usgs.gov/landsat-missions/landsat-satellite-missions.

For more information about this publication, contact:
Director, USGS Earth Resources Observation and Science Center
47914 252nd Street
Sioux Falls, SD 57198
605–594–6151

For additional information, visit: https://www.usgs.gov/centers/eros

Publishing support provided by the
USGS Science Publishing Network
Rolla and Baltimore Publishing Service Centers

ISSN 2331-1258 (online)
https://doi.org/10.3133/ofr20211030W